

PHY  
873

This work is submitted as a dissertation to the department of physics,  
Quaid-i-Azam University Islamabad, in the partial fulfillment of the  
requirement for the degree of

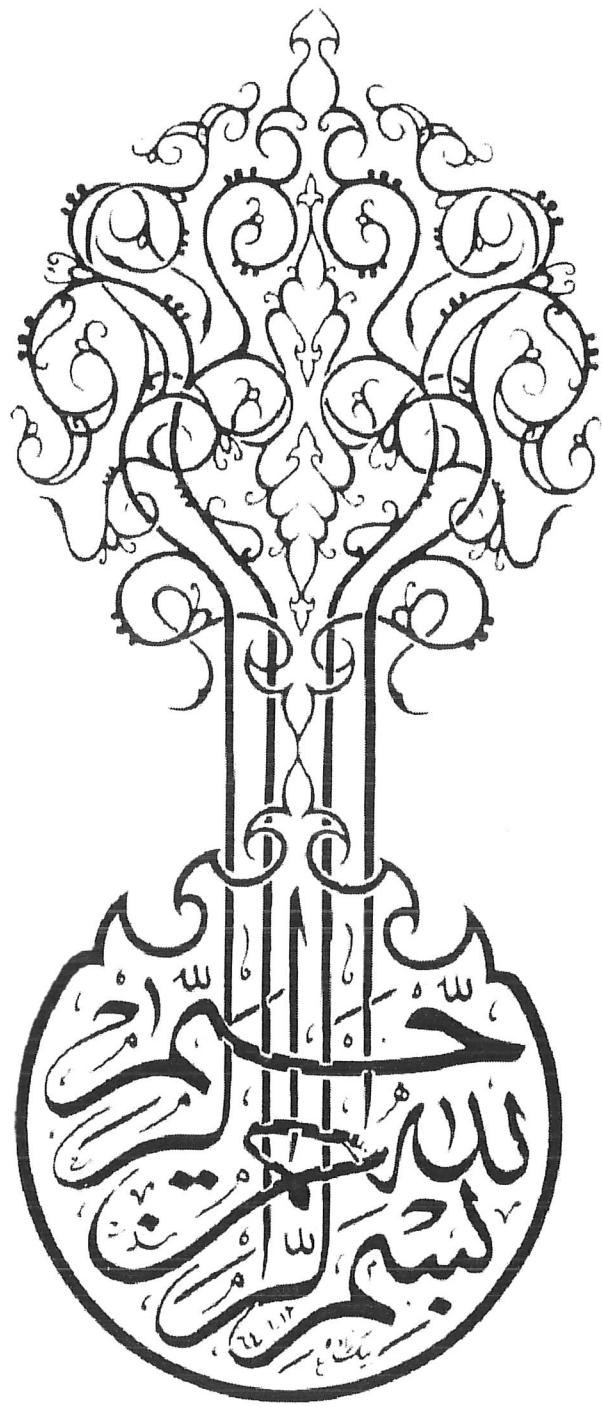
## **Master of Philosophy**

In

## **Physics**



**Department of Physics**  
**Quaid-i-Azam University**  
**Islamabad, Pakistan**  
**2011**



# CERTIFICATE

---

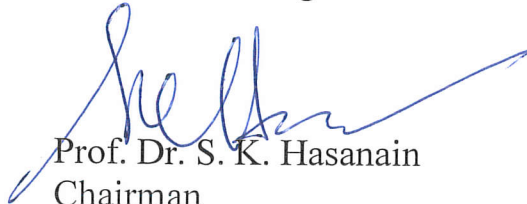
It is certified that the work contained in this thesis is carried out and completed under my supervision at the Atomic & Molecular Physics Laboratory, Department of Physics. Quaid-i-Azam University, Islamabad, Pakistan.

*Raheel Ali*

Dr. Raheel Ali  
(Supervisor)

Assistant Professor  
Atomic & Molecular Physics Laboratory  
Quaid-i-Azam University  
Islamabad, Pakistan.

Submitted through:



Prof. Dr. S. K. Hasanain  
Chairman  
Department of Physics  
Quaid-i-Azam University  
Islamabad, Pakistan.

*.....to my loving  
parents,  
family members  
&  
respected  
teachers*

# CONTENTS

---

<b>Acknowledgements</b>	<b>III</b>
<b>Abstract</b>	<b>V</b>
<b>List of figures</b>	<b>VI</b>
<b>List of tables</b>	<b>VIII</b>
<b>Chapter 1      Introduction</b>	<b>1</b>
1.1 <b>Spectroscopy</b>	<b>1</b>
1.1.1    Overview	1
1.1.2    Applications of Spectroscopy	2
1.2 <b>Spectra of Rare Gases</b>	<b>3</b>
1.2.1    Coupling Schemes for the Rare Gases	3
1.3 <b>Rydberg Atoms</b>	<b>5</b>
1.3.1    Properties of Rydberg Atoms	6
1.3.2    Excitation of Rydberg States	7
1.3.3    Detection of Rydberg Atoms	7
1.4 <b>Excitation Schemes</b>	<b>8</b>
1.4.1    Single-Step/Single-Photon Excitation	8
1.5 <b>Lay out of the Thesis</b>	<b>9</b>
<b>Chapter 2      Theoretical Aspects</b>	<b>11</b>
2.1 <b>Laser Spectroscopy</b>	<b>11</b>
2.2 <b>Optogalvanic Spectroscopy</b>	<b>12</b>
2.2.1    Advantages of Optogalvanic Spectroscopy	13
2.2.2    Applications of the Optogalvanic Spectroscopy	13
2.3 <b>Rate Equation Model</b>	<b>14</b>
2.3.1    Rate Equations	16
2.3.2    Instrumental Time Constant	18
2.3.3    Effect of Discharge Current	18
<b>Chapter 3      Experimental Setup</b>	<b>20</b>
3.1 <b>Introduction</b>	<b>20</b>
3.2 <b>Nd: YAG Laser</b>	<b>20</b>
3.3 <b>Dye Lasers</b>	<b>23</b>
3.3.1    Resonant Cavity	24
3.3.2    Molecular Transitions and Spectra	25

<b>3.4</b>	<b>Hollow Cathode Lamp</b>	<b>26</b>
3.4.1	Limitations of Hollow Cathode Lamp	26
<b>3.5</b>	<b>Fabry-Parot Etalon</b>	<b>27</b>
<b>3.6</b>	<b>Photodiode</b>	<b>28</b>
<b>3.7</b>	<b>Data Acquisition System</b>	<b>28</b>
3.7.1	Boxcar Averager	28
3.7.2	Oscilloscope	29
3.7.3	PC Recorder	29
<b>Chapter 4</b>	<b>Results and Discussions</b>	<b>31</b>
<b>4.1</b>	<b>Introduction</b>	<b>31</b>
<b>4.2</b>	<b>Energy Levels</b>	<b>32</b>
4.2.1	Time-Resolved Optogalvanic Spectroscopy	33
<b>4.3</b>	<b>Experimental Results</b>	<b>35</b>
4.3.1	Case-1 ( $\Delta J = -1, \Delta K = 0$ )	35
4.3.1a	Lengthening of the Effective Life Time of the Upper Level	38
4.3.1b	Effective Electron Collisional Ionization Rate Parameter	39
4.3.2	Case-2 ( $\Delta J = 1, \Delta K = 0$ )	40
4.3.3	Case-3 ( $\Delta J = \Delta K = 0$ )	43
<b>Conclusion</b>		<b>50</b>
<b>Bibliography</b>		<b>51</b>

# ACKNOWLEDGEMENTS

---

I fully realize the blessings upon me by the most gracious and divine force of all the forces, without whom the mere existence of my being is impossible. I don't have the words to explain my gratitude to the **Almighty Allah**, who gave me the vision and insight to acquire knowledge and to materialize this research work. I offer my humblest and sincerest words of thanks to our **Holy Prophet (P.B.U.H.)** who is like a beacon in every aspect of life whether it is the purpose of education or how to work in a group

Building this experimental work had not been an easy task, but there are those who worked with me, who made the experience somewhat less painful and this section is dedicated to them without whom this thesis would never be completed.

First of all, I would like to thank **Dr. Raheel Ali** for having faith in me and giving me a chance to work in his lab at a time when it was not clear that I had any experimental talents. I consider myself extremely lucky to have had **Dr. Raheel Ali** as my M. Phil supervisor; he is a true master of experimental physics. His crystal clear explanation of physical principles has allowed me to grasp difficult concepts with relative ease. Not only was his guidance critical to the success of this study, but his company has made it a very enjoyable experience. Sir, thank you very much for teaching me all that you have done, feeding back on this dissertation and for putting up with me.

I am delighted to interact with **Prof. Dr. Aslam Baig (S.I, T.I, H.I)\*** by attending his classes and having him as my co-advisor in the laboratory. His insights to experimental setups are second to none. Besides, he sets an example of a world-class researcher for his rigor and passion on research.

I also appreciate the support from **Prof. Dr. S. K. Hasanain**, the Chairman of Physics department, which helped us in completing this assignment within the stipulated time.

My immense gratitude goes to all the teachers of physics department especially to **Dr. Pervez A. Hoodbhoy, Dr. Zakullah, Dr. Tasneem Zahra Rizvi** and **Dr. Umar Saeed Qurashi**, I can never forget the best guidance granted by them.

\* S.I. Sitara-e-Imtiaz, T.I. Tamgha-e-Imtiaz and H.I. Hilal-e-Imtiaz

I would also like to thank **Dr. Naveed Khaliq Piracha** (John Carroll University, USA) for giving me his precious time and for putting me right on the fittings of the given results.

I owe special thanks to **Dr. Xianming L. Han** (Butler University, Indianapolis, USA) for fruitful discussion on the subject especially his help on the mathematical rate equation model given by him.

All my lab buddies at the Atomic & Molecular Physics Laboratory made it a convivial place to work. In particular, I would like to thank Ijaz Bokhari for his friendship and help in the past one year. All other folks, including, Ashiq Fareed, Syed Jarrar Gardezi, Abdul-Wahab, Rauf Shahzad, Sumera Khizar, Zahid Imroz & Oun-ul-Haq are inspired me in research and life through our interactions during the long hours in the lab, Thanks.

Every human being is born with a motive, an aim, and a purpose, everyone has to live that purpose before he or she makes an exit from this world. The journey to this destination is tough and challenging filled with stones but if we have good friends to travel along we can do wonders. The same blocking stones can then be used to make a bridge that will help us take a step further. I would like to dedicate these sentences to all my friends specially, Atta-ur-Rahman, Shahidullah, Muhammad Ilyas, Rahmat Zia, Muqaddar Abbas, Sardar Badshah, Mehar Ali Shah, Saadi Ishaq, Muhammad Abid, Rashid Khan, Hazrat Bilal, Muhamad Ibrahim, Muhammad Rahim, Faiq Jan, Fariha Adeel, Tayyaba Aftab, Haseen Ullah, Kamran Khan, Sumeera Sarwar, Humaira Younis and my roommate Muhammad Imran.

Special thanks to my cousin Hamdullah for guiding and helping me in writing this dissertation.

I would also wish to appreciate my brother **Lt. Col. Jamal** for encouraging, motivating me and for his financial support throughout my studies.

Last but not the least: I offer my deepest and heartiest gratitude to my parents, brothers, sisters and all of my family members for their prayers, encouragements and well wishes. Their love always heartens me to achieve success in my life.

Syed Zaheer-ud-Din



# ABSTRACT

---

In the present work we have studied the dominant physical processes responsible for the production of the optogalvanic signal in the spectra of Xenon. A locally fabricated dye laser system pumped by a Nd:YAG laser system was used for the optogalvanic spectroscopy. A commercial hollow cathode was used to populate the  $5p^56s$  states of Xenon through collision. We have investigated the effects on the optogalvanic signal by scanning a dye laser across the Xenon transitions in this hollow cathode lamp. Time-resolved spectra are recorded at a fixed wavelength of the dye laser resonantly tuned to an optically allowed single photon transition. We kept the dye laser energy fixed for a particular transition. The temporal evolutions of the signals are recorded on a storage oscilloscope. Two transitions from the metastable state  $6s[3/2]_2$ , and one transition from the  $6s[3/2]_1$  state corresponding to  $\Delta J = \Delta K = 0, \pm 1$  dipole selection rules, have been selected to investigate the dominant physical processes responsible for the optogalvanic signals. The change in the signal amplitude as a function of the discharge current has been registered. In addition the electron collisional ionization rate parameter ratios have been determined for the transitions corresponding to the dipole selection rules,  $\Delta J = -1$   $\Delta K = 0$ ,  $\Delta J = 1$   $\Delta K = 0$  and  $\Delta J = \Delta K = 0$  as 23, 1.2 and 12.4 respectively. The effective lifetimes of the upper levels involved in the previously mentioned transitions are also calculated as  $0.33 \mu s$ ,  $0.28 \mu s$  and  $0.06 \mu s$  respectively. Lengthening of the effective lifetime is also explained in the light of the various mechanisms involve in the discharge.

# LIST OF FIGURES

---

<b>Figure 1.1:</b>	Single-step/Single-photon excitation.	9
<b>Figure 2.1:</b>	Energy diagram showing transitions and dynamics involved in the OG signals.	16
<b>Figure 3.1:</b>	Schematic diagram of the experimental setup.	21
<b>Figure 3.2:</b>	Energy levels in Nd: YAG laser.	22
<b>Figure 3.3:</b>	A Hanna type dye laser.	25
<b>Figure 3.4:</b>	Energy level diagram for molecular transitions.	26
<b>Figure 3.5:</b>	Xenon filled hollow cathode lamp.	27
<b>Figure 3.6:</b>	A Fabry-Perot Etalon.	28
<b>Figure 4.1:</b>	Partial energy level diagram for Xenon transitions.	33
<b>Figure 4.2:</b>	Observed and fitted optogalvanic signal at 2 mA discharge current of two de-convoluted signals.	34
<b>Figure 4.3:</b>	Time-resolved optogalvanic signals of Xenon at 469.22 nm following the $\Delta J = -1$ , $\Delta K = 0$ selection rules.	35
<b>Figure 4.4:</b>	Set of time-resolved optogalvanic signals registered at different discharge currents.	36
<b>Figure 4.5:</b>	Plot of the optogalvanic signal amplitude vs discharge current.	37
<b>Figure 4.6:</b>	Plot of the decay rates vs the discharge current.	38
<b>Figure 4.7:</b>	Time-resolved optogalvanic signals of Xenon at 473.54 nm corresponding to $\Delta J = 1$ , $\Delta K = 0$ selection rules.	41
<b>Figure 4.8:</b>	Set of time-resolved optogalvanic signals compiled at different discharge currents ranging from 2 mA to 5.5 mA.	41
<b>Figure 4.9:</b>	Plot of decay rates vs discharge current for Xenon 473.54 nm.	42
<b>Figure 4.10:</b>	Plot of the signal amplitude vs discharge current for Xenon 473.54 nm.	42
<b>Figure 4.11:</b>	Time-resolved optogalvanic signals of Xenon at 452.6 nm	

corresponding to $\Delta J = \Delta K = 0$ selection rules.	44
<b>Figure 4.12:</b> Set of time-resolved optogalvanic signals compiled at different discharge currents ranging from 2.5 mA to 6 mA.	44
<b>Figure 4.13:</b> Plot of decay rates vs discharge current for Xenon 452.6 nm.	45
<b>Figure 4.14:</b> Plot of the signal amplitude vs discharge current for Xenon 452.6 nm.	45

# LIST OF TABLES

---

<b>Table 4.1:</b>	Data for time-resolved OG signals of Xenon at 469.22 <i>nm</i> for different discharge currents.	46
<b>Table 4.2:</b>	Data for time-resolved OG signals of Xenon at 473.54 <i>nm</i> for different discharge currents.	47
<b>Table 4.3:</b>	Data for time-resolved OG signals of Xenon at 452.6 <i>nm</i> for different discharge currents.	48
<b>Table 4.4:</b>	Results.	49

# CHAPTER 1

---

## Introduction

### 1.1 Spectroscopy

#### 1.1.1 Overview

Spectroscopy deals with properties of matter through its interaction with its different frequency components of electromagnetic spectrum. It is basically an experimental technique that uses the interaction of energy with a sample to perform analysis. It consists of two words, one is the Latin word “spectron” means “ghost” and other is the Greek word “scope” means “to see”.

The earliest reference to optical spectroscopy that we have in modern times appears to be the phenomenon of colours in Isaac Newton's Optics, in which he describes his famous experiments with prisms, and the shaft of sunlight coming through the hole in his window shutter. There was much philosophical conjecture at the time, but in 1802 the British scientist William Wollaston discovered the existence of dark lines in the solar spectrum. Thirteen years later, Josph von Fraunhofer repeated Wollaston's work, and hypothesized that the dark lines were caused by an absence of certain wavelengths of light [1]. It was not until 1859, however, when German physicist Gustav Kirchhoff was able to successfully purify substances, and conclusively show that each pure substance produces a unique light spectrum. Kirchhoff went on to develop a technique for determining the chemical composition of matter using spectroscopic analysis that he, along with Robert Bunsen, used to determine the chemical make up of the sun.

The end of the nineteenth, and beginning of the twentieth centuries was marked by significant efforts to quantify and explain the origin of spectral phenomena. Beginning with the simplest atom, hydrogen, scientists including Johann Balmer and Johannes Rydberg developed equations to explain the atom's frequency spectrum. It was not until Niels Bohr developed his famous model in 1913 that the energy levels of the hydrogen spectrum could accurately be calculated. However, Bohr's model failed miserably when

applied to other elements that had more than one electron. It took the development of quantum mechanics by Werner Heisenberg and Erwin Schrödinger in 1925 to universally explain the spectra of most elements.

From the discovery of unique atomic spectra developed modern spectroscopy. The three main varieties of spectroscopy in use today are absorption, emission, and scattering spectroscopy. Absorption spectroscopy measures the wavelengths of light that a substance absorbs to give information about its structure. Emission spectroscopy measures the amount of light of a certain wavelength that a substance emits. Lastly, scattering spectroscopy is similar to emission spectroscopy but detects and analyses all of the wavelengths that a substance reflects upon excitation [2].

### 1.1.2 Applications of Spectroscopy

Spectroscopy is a useful tool for analyzing the composition of an unknown substance. It is used to determine identity, quantity, structure, and the environment of atoms, molecules, and the ions. It involves the investigation of interaction of light with matter; a spectrum shows how this interaction varies with the frequency of the light.

The primary applications of spectroscopy are the following:

- ❖ Spectroscopy is used to unfold the spectra of complex atoms and highly complex series, to determine their transition probabilities, hyperfine structures and isotopic shifts.
- ❖ It is useful to develop the theories of many-body as well as understanding of recombination and scattering processes from the complex spectra of atoms.
- ❖ Another important application of spectroscopy is to find the interactions between atoms, molecules, photons and ions, to determine intensities and widths of spectral lines.
- ❖ Spectroscopy is also used to identify the atoms, their structures and the environment of the atoms and molecules.
- ❖ The modern spectroscopy underlines the mechanism of some lasers, the accurate measurement of frequencies, the cooling of atoms to sub-micro-Kelvin temperatures, and also radio and optical Astronomy.

## 1.2 Spectra of Rare Gases

The rare gases belong to the group of atoms which have a closed shell in the ground state configuration, resulting in a  $^1S_0$  ground state. This configuration makes the rare gases spectra qualitatively different from the alkali and alkali earth elements. The separation between the ground state and the ionization potential is about 4 eV for alkali and  $\sim 12$  to 24 eV for rare gases. The rare gases (except He) have an  $ms^2mp^6$  closed shell configuration therefore singly excited state consists of an electron outside the ionic core which has a double fine structure splitting  $^2P_{3/2}$  and  $^2P_{1/2}$ . Consequently, there are two distinct sets of singly excited series converging to two ionization limits  $mp^5^2P_{3/2}$  and  $mp^5^2P_{1/2}$ , where m stands for 2, 3, 4, and 5 for Neon, Argon, Krypton, and Xenon respectively.

Alkali atoms can be easily excited to the first excited state by a single photon of energy  $\sim 2$  eV, while for the excitation from the ground state of rare gases, one needs photons of energy  $\sim 8$  to 20 eV. This makes the optical excitation of rare gases extremely difficult unless one uses the multiphoton processes. A way to avoid this difficulty in rare gases is to use discharge, in which metastable levels are populated through collisions. The photo excitation from these metastable levels can proceed as that of the alkali atoms. This excitation process for the rare gases forms the core of the present studies.

### 1.2.1 Coupling Schemes for the Rare Gases

The way in which the angular momenta are coupled in an atom has important bearing on the structure of the spectra. For the atoms of smaller atomic numbers, the predominant coupling is the  $LS$  coupling. In  $LS$  coupling scheme the electrostatic interaction between electrons are stronger than the magnetic interaction (spin orbit). The orbital angular momenta  $l_i$  (where  $i = 1$  to  $n$ ) of the electrons are coupled to form the total angular momentum  $L$ :

$$L = \sum_{i=1}^N l_i \quad 1.1$$

The spin angular momentum  $s_i$  of each electron coupled to form the total angular momentum  $S$ :

$$S = \sum_{i=1}^N s_i \quad 1.2$$

The total angular momentum  $J$  is given by:

$$J = |L \pm S| \quad 1.3$$

The state in  $LS$  coupling scheme is designated by  $^{2S+1}L_J$  where  $2S+1$  is the multiplicity of the state.

In heavy atoms the magnetic interaction is stronger than the electrostatic interaction between the electrons resulting in each electron's spin coupling to its orbital angular momenta namely:

$$j_i = |l_i \pm s_i| \quad 1.4$$

Each  $j_i$  are then coupled to form  $J$ , the total angular momentum:

$$J = \sum_i j_i \quad 1.5$$

This coupling is called  $jj$  coupling scheme. The states with given values of  $j_1 j_2$  and  $J$  are denoted by means of  $(j_1 j_2)_J$ .

Apart from the above mentioned frequently used coupling schemes ( $LS$  and  $jj$ ), the other popular coupling scheme is the intermediate scheme or  $Jl$  coupling scheme [3,4]. The energy levels of most of the elements when the optical electron is on average at a greater distance from the electrons of the atomic core are characterized by this scheme. In this scheme the orbital angular momentum  $l$  of the excited electron couples with the total angular momentum  $j_c$  of the core to give the resultant angular momentum  $K$ :

$$K = |j_c \pm l| \quad 1.6$$

The angular momentum  $K$  is then weakly coupled with the spin angular momentum  $s$  of the Rydberg electron to give the angular momentum  $J$ :

$$J = |K \pm s| \quad 1.7$$

In  $jl$  coupling scheme the states are denoted as  $nl[K]_J$ .

The rare gases (except He) are most conveniently described by this intermediate coupling scheme. Since there are two states of the ionic core corresponding to two different values of the angular momentum  $j_c$ , therefore, there are two distinct sets of the excited states



depending on  $j_c$ . These sets are generally denoted by  $nl[K]_J$  (for  $j_c = 3/2$ ) and  $nl'[K]_J$  (for  $j_c = 1/2$ ).

### 1.3 Rydberg Atoms

*“Once the Bohr’s Theory was formulated it was apparent that Rydberg atoms should have bizarre properties.”* Thomas F. Gallagher, *Rydberg atoms*

The Rydberg atoms due to their unusual properties and possible practical applications have become a topic of immense interest in the field of spectroscopy [5,6]. The study of these atoms have provided much deeper insights in the understanding of the atomic structure and have stimulated new theoretical calculations. This is the reason that an enormous data on Rydberg atoms covering a large number of atomic species from Helium to Uranium exists.

In an atom when the valence electron is excited, from the ionic core, to an orbit with large principal quantum number  $n$ , a Rydberg atom is formed. The excited electron sees the nucleus and the core electrons as a point charge  $e^+$ . This configuration of the atom can be treated by simple Hydrogen like model and the energy levels of such an atom can be calculated by the Rydberg–Ritz formula. The Rydberg energy levels are different from the hydrogenic levels. This discrepancy which is more for low  $n$  values, from the hydrogenic behavior provides information about the properties of the atomic core and its interaction with the Rydberg electron. A Rydberg electron spends most of its time far from the ionic core where the effective potential is essentially coulombic given by

$$V_{(r)} \cong -\frac{e^2}{r} \quad 1.8$$

Where  $r \geq r_0$ ,  $r_0$  is the radius of the region around the nucleus which limits the core wavefunction. For the low angular momentum orbits i.e. penetrating orbits, the Rydberg electron experiences the unshielded nuclear charge (non-coulombic interaction), and is more tightly bound which lowers the energy levels from the hydrogenic values. The higher angular momentum  $\ell$  states though exhibit very little core penetration, actually cause core polarization. This is the result of the electric field of the electron at the ionic core, which distorts the polarizable core leading to a negative energy shift. The

magnitude of the energy shift due to the core polarization is smaller than the shift caused by the core penetration. This depression in the energies of Rydberg levels is the measure of the quantum defect  $\mu$ . The value of  $\mu$  decreases with increasing  $\ell$  and increases with atomic number  $Z$  for a given  $\ell$  value. For the hydrogen atom, the value of  $\mu$  is zero. The effect of core polarization and core penetration is very well studied and is described by the Multichannel Quantum Defect Theory (MQDT).

### 1.3.1 Properties of Rydberg Atoms

Some interesting properties of these states are listed below:

- ❖ The energy levels of the Rydberg atoms with principal quantum 'n' and orbital angular momentum ' $\ell$ ' are represented by the formula,

$$E_{n,\ell} = IP - \frac{R}{(n - \mu_\ell)^2} \quad 1.9$$

Where  $R$  is the Rydberg Constant,  $\mu_\ell$  is the quantum defect of the level and it depends on the angular momentum ' $\ell$ ' of the excited electron. It describes the measure of the core penetration.

- ❖ The binding energies of Rydberg atoms are very low. It requires very small amount of energy to be ionized. It is proportional to  $\frac{1}{n^2}$ .
- ❖ Their size is enormous on the atomic scale and is directly proportional to  $n^2$ , i.e.,  $\langle r \rangle = a_0 n^2$  where  $a_0$  is the Bohr radius.
- ❖ Their geometrical cross-section is very large,  $\sigma_g = (\pi a_0^2 n^4)$ .
- ❖ Highly excited Rydberg atoms possess relatively long lifetime, i.e.,  $\tau_n$  is proportional to  $n^3$ .
- ❖ The energy separation  $\Delta E$  between adjacent levels is given for large  $n$  values as,

$$\Delta E = E_{n+1} - E_n = \frac{2R}{n^3} \quad 1.10$$

### 1.3.2 Excitation of Rydberg States

There are different mechanisms used for the excitation of Rydberg states. These include electron transfer [7], electron bombardment [8] and photoabsorption techniques [9]. The absorption spectroscopy of Rydberg atoms, with classical light sources, remained restricted to the excitation of few low lying levels, particularly those accessible by electric dipole transitions from the ground state. The selective excitation of Rydberg atoms have to wait till the advent of tunable laser sources.

The tuneability and high spectral density over the entire optical spectrum of dye lasers have opened new vistas in Rydberg state spectroscopy. The number of high lying atomic states accessible to experiments has been considerably increased due to the inclusion of different excitation schemes like multicolor and multiphoton excitation. For those atoms which have low ionization potentials, e.g. alkalis, one step excitation from the ground state is possible (with/without frequency doubling the dye laser output). Whereas, for elements with high ionization potentials, e.g. noble gases, one step excitation requires VUV photons. The difficulty can be overcome by populating the low lying metastable states in a discharge and from there the tunable optical excitation can be used to populate the Rydberg states [10,11].

### 1.3.3 Detection of Rydberg Atoms

There are different techniques for the detection of Rydberg atoms, which are given below:

#### ❖ Field Ionization

This is a very important mechanism for the selective detection of Rydberg atoms. By applying a certain external field ( $E_{critical}$ ) to the highly excited Rydberg states, the ionization potential can be lowered and the field ionization may occur. Different field values ionize different states, which can readily be detected. The electric field required to ionize valence electron increases approximately as the square of the binding energy of the atom. This can be expressed by  $E_{critical} = \frac{1}{n^4}$ .

## ❖ Fluorescence Detection

This technique is noticeable for detecting Rydberg states, which have large collisional cross-sections and long radiative lifetimes. The collisional decay at the required particle densities therefore become more probable than the radiative decay rates of these high lying states.

## ❖ Collisional Ionization in a Space Charge Limited Diode

This is an efficient technique to study the highly excited atomic states [12,13]. The space charge surrounding the cathode gets modified when an electron is created in its vicinity-giving rise to a current pulse.

## ❖ Optogalvanic Technique

This detection method has very attractive characteristics namely, simplicity and high sensitivity. We have employed this detection technique to study the time resolved spectra of Xenon. A detail discussion on optogalvanic detection mechanisms is given in article (2.2).

## 1.4 Excitation Schemes

When an atom absorbs energy and promoted from its lower level to an upper level this phenomenon is called excitation. There are different types of excitation schemes used in the laser spectroscopy that is, single-step/single-photon excitation, multi-step photo excitation and multi-photon excitation, which depends upon the photon energy available and the parity of the involved states. Here in our work we used the single-step/single-photon excitation scheme and is briefly described below.

### 1.4.1 Single-Step/Single-Photon Excitation

In a single-step photoexcitation, the outermost electron of an atom undergoes a transition from some initial discrete state  $|i\rangle$  of energy  $E_i$  to another discrete state  $|f\rangle$  of higher energy  $E_f$  by absorbing a photon of a particular energy “ $h\nu$ ” following the relation:

$$E_f - E_i = h\nu_{if} \quad 1.11$$

Here  $h$  is the Planck's constant and  $\nu_{if}$  is the frequency of the absorbed photon. Similarly, when an electron jumps from higher energy state to a lower energy state, a photon of energy equal to the energy difference of the two states is emitted. A simple explanation of single-step excitation is shown in figure (1.1).

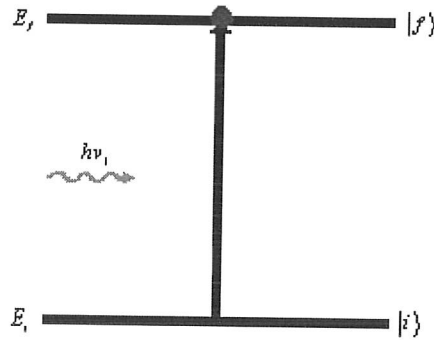


Fig: 1.1 Single-step/Single-photon excitation.

The single-step photoexcitation process obeys the electric dipole transition selection rules  $\{\Delta l = \pm 1, \Delta S = 0, \text{ and } \Delta J = 0, \pm 1 (0 \not\leftrightarrow 0)\}$ , where  $l$  is the orbital angular momentum,  $J$  is the total angular momentum and  $S$  is the multiplicity of the concerned states. The transition probability per unit time for single-step photoexcitation, using the electric dipole approximation [14], is expressed as

$$P_{if} = \frac{4\pi^2}{3\hbar^2} \frac{\rho(\omega_{if})}{4\pi\epsilon_0} |\langle f | er | i \rangle|^2 \quad 1.12$$

Here  $\rho(\omega_{if})$  is the radiation density per unit interval of the angular frequency. The transition probability depends on the electric dipole matrix element  $|\langle f | er | i \rangle|^2$ . The parity between the initial and the final state must change in order to have this term to be non-zero. In a single-electron atom excitation this requires that the angular momentum must change by  $\pm 1$ .

## 1.5 Lay Out of the Thesis

Chapter two presents briefly the theoretical aspects of laser spectroscopy, optogalvanic spectroscopy, and the rate equation model. Chapter three describes the experimental

setup. Chapter four concludes the results and discussions of the time-resolved optogalvanic spectra of Xenon.

# CHAPTER 2

---

## Theoretical Aspects

### 2.1 Laser Spectroscopy

Before 1960, scientists were using broad band background conventional sources for the spectroscopic analysis. These sources were providing wide energy bands for atomic transitions. A major part of this energy would be absorbed by the medium as kinetic energy which would cause to raise the temperature. Therefore these conventional methods failed to obtain high resolution spectrum. The first laser, in 1960, was produced by Theodore Maiman of Hughes Research Laboratories using a Ruby laser and a flash lamp as a pumping source. The invention of laser has proved very useful in spectroscopy and is being extensively used these days to obtain high resolution spectra [15]. Helium-Neon laser, a continuous-wave gas laser emitting infra red light at  $1.15 \mu m$  was developed by Javan 1961 [16] of Bell Laboratories. Later on Johnson [17] and Nassau [18] made the first Neodymium laser at the same laboratory. In order to improve the control, operation and reliability of lasers, many special cavity arrangements, feed back schemes and other devices were also developed [19].

A laser consists of following three main parts:

- ❖ A gain medium that can amplify light that passes through it.
- ❖ An energy pump source to create a population inversion in the gain medium.
- ❖ Two mirrors which form a resonator cavity.

The advantages of laser over the conventional sources are due to its directionality, monochromaticity, coherence and brightness. Laser light due to its high intensity, narrow line width of the spectral lines and phase coherence, immediately stimulated new interest in atomic and molecular spectroscopy. Intense laser light has opened the field of non-linear optics, the formalism of which was developed by Bloembergen [20]. Frequency mixing processes such as second harmonic generation were discovered and exploited to generate coherent light at new wavelengths deep in the ultra-violet and far infrared. Other

non-linear optical effects studied include the stimulated Raman effect, four-wave mixing and other stimulated processes induced by the high intensities of laser light (large number of photons per mode). Multi-photon absorption in atoms was used to ionize and detect trace quantities, and multi-photon absorption in molecules was used to produce large quantities of highly excited state species.

New results in laser spectroscopy continue to advance the field. The developments of atom traps, combined with laser slowing of atomic beams due to photon recoil, called laser cooling, has led to techniques for highly localized confinement of isolated atoms. These species, trapped in space, can then be studied free of the usual external perturbations, providing spectroscopic data of extremely high resolution for fundamental studies and applications.

## 2.2 Optogalvanic Spectroscopy

When a self-sustained gaseous discharge is illuminated by radiation resonant with an atomic or molecular transition of the element within it, a change in its electrical properties occurs. This change observed as an increase or decrease in the conductivity of the discharge and is known as “the optogalvanic effect” (OGE).

The OGE was first described by Penning in 1928 [21], who noted a variation in the impedance of a neon discharge when it was irradiated by an emission from an adjacent Neon discharge. Similar observations were later made on Hg and He discharges by Kenty in 1950 [22] and Meissner and Miller in 1953 [23]. In all cases the pumping effect of the radiation on the metastable levels, which are critically involved in the ion-electron production mechanism inside the discharge, made it possible to observe this phenomenon by using incoherent light sources. Extensive and practical applications of the OGE had to wait for the introduction of tunable dye lasers.

The actual development of the OGE as a useful spectroscopic tool began with the work of Green, Keller, and Luther [24]. They irradiated a discharge using a tunable dye laser and demonstrated that high-sensitivity spectra of the species present in the discharge could be obtained. The electronic excitation of the atoms in the discharge allowed for the observation of transitions starting from the metastable or excited states, while the use of a



hollow-cathode discharge made it possible to perform spectroscopy on a gas-phase sample of refractory elements produced by cathodic sputtering.

The OG technique can be considered as an alternative to absorption or fluorescence techniques. The experimentally observed perturbation of the discharge characteristics induced by laser radiation (even at high saturation level) is usually sufficiently small so that OGE can be considered directly proportional to the number of photons absorbed [25].

### 2.2.1 Advantages of Optogalvanic Spectroscopy

OG spectroscopy gets importance the absorption and fluorescence studies of the spectroscopic data. Absorption spectroscopy is limited to the sample that has sufficient optical density to absorb a detectable amount of the incoming radiation. Fluorescence spectroscopy can often be used to study weakly absorbing sample, but this technique also has a few limitations. The sample may fluoresce at a wavelength beyond the range of a particular detector (such as in the vacuum ultraviolet). It may fluorescence through many “decay channels”, only one of which may be convenient to monitor. The excited states may decay primarily through non-radiative processes etc.

OG spectroscopy is less expensive and involves the use of fewer electronics than the usual optical detection techniques. With regards to signal to noise, ratio, the current noise in the discharge can be reduced practically to the shot noise i.e., when the discharge operates in the correct regime.

### 2.2.2 Applications of the Optogalvanic Spectroscopy

The OGE has many applications some of which are given below:

- ❖ The easy detection and high sensitivity of Laser OGE has offered a variety of applications for laser spectroscopy. This effect is very efficient in the detection of trace elements.
- ❖ The OG technique has been applied extensively in the study of Rydberg states. These can be reached by exciting the radiative transitions starting from the metastable states, which are well populated in the discharge. This is particularly

true for the noble gases and for the alkaline-earth atoms.

- ❖ The OGE has been used, for the wavelength calibration and the frequency stabilization of pulsed or cw dye lasers in any spectral region. It can also be used for the determination of the dye laser bandwidth.
- ❖ The OGE can be used to determine the relative oscillator strengths of different levels and the electron temperature of the discharge.
- ❖ The OGE can be employed to detect the transition between electronically excited levels in the atoms, molecules, free radicals and refractory elements.
- ❖ The isotopic splitting can also be observed with the OG spectroscopy.
- ❖ The OGE can be used very successfully as a tool for learning about the discharge mechanisms. A very useful data on the structure of the cathode fall was obtained with this technique. Detection through OGE produces a better signal-to-noise ratio, in the cathode fall region as compared to any other fluorescence or absorption methods.
- ❖ The OGE can be used to study the kinetics of the fast reaction.
- ❖ The OGE is very efficient for the investigation of the autoionization levels.
- ❖ The OGE can be used as a diagnostic tool for the study of low energy plasmas.
- ❖ The OGE technique can be used effectively in the investigation of hyperfine structure of the atoms.

## 2.3 Rate Equation Model

OGE in the rare gases has been widely studied and different models have proposed to account for this effect [26,25,27]. These models characterize the response of the discharge, when the steady state population distribution of the levels, is perturbed by a laser resonant to a transition between these levels. A simple phenomenological model based on the multiplication of an electron in the plasma can be constructed to describe the OG signal and its time dependent behaviour [27]. In DC discharge plasma, an electron emitted from the cathode and traveling towards anode can generate electrons in the medium by excitation and ionization mechanisms. The resulting ions move towards cathode and in this process more electrons are liberated in the medium. An avalanche is thus initiated by the inclusion of a single electron in the discharge.

Stewart Constructed a rate equation model for the OGE in the positive column of the neon glow discharge [28]. This model includes the ground state atom and electron collisional coupling processes. It was demonstrated that the electron transfer plays a dominant role in determining the magnitude and sign of the OGE. Han [29] presented a theoretical model, which quantitatively characterizes the dominant physical processes responsible for the OG signal in the discharge plasma. This model, with only five parameters, reproduces the experimentally obtained time-resolved OG signals.

The present work quantitatively characterizes the dominant physical processes contribution to the OG signal in the discharge plasma. When the laser is tuned to a Xenon transition, the observed OG signal intensity as a function of time,  $S(t)$ , is the sum of signals originating from all the energy states involved;

$$S(t) = S_i(t) + S_k(t) + \sum S_j(t) \quad 2.1$$

Where  $S_i$  and  $S_k$  are the contribution from the lower state  $i$  and the upper state  $k$  associated with the laser excitation, respectively. In addition to  $i$  and  $k$  states which are directly involved in the optical excitation, contribution to the OGE, signal may also arise as a result of transition from state  $k$  to an intermediate state  $j$ . If there is only one lower state  $i$  to which the state  $k$  can decay, then equation (2.1) is reduced to only two terms. A simplified two-level energy diagram is shown in figure (2.1) to illustrate the dynamics considered in the present model.

By laser excitation, the number of atoms in either state is mainly determined by three processes;

- ❖ Electron collisional excitation
- ❖ Radiative depopulation
- ❖ Electron collisional ionization

The electron collisional excitation from the ground state  $^1S_0$  to  $i$  and  $k$  states depends on the discharge current  $I$  and the corresponding scale factors  $P_i$  and  $P_k$ . These factors involve all the electron collisional processes that contribute to the steady-state populations of these states. The radiative depopulation is governed by populations ( $N_i$  and

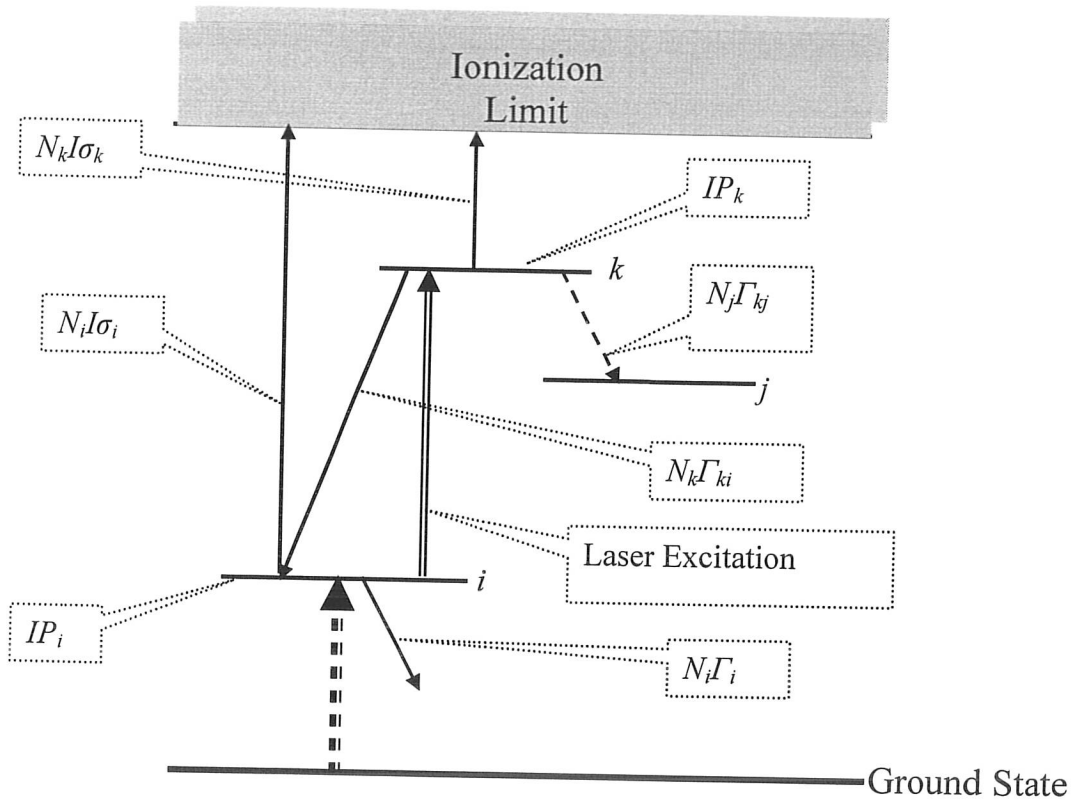


Fig: 2.1: Energy diagram showing transitions and dynamics involved in the OG signals.

$N_k$ ) and the effective decay rates ( $\Gamma_i$  and  $\Gamma_k$ ) for each state. The observed OG signal comes from the electron collisional ionization.



Where  $A^*$  and  $A^+$  are excited metastable and ionization states respectively.

The shape and the intensity of the OG signal depends on  $N_i I \sigma_i$  and  $N_k I \sigma_k$ , where  $I$  is the discharge current and  $\sigma_i$  and  $\sigma_k$  are the electron collisional ionization rate parameters. They are proportional to the electron collisional ionization cross section of  $i$  and  $k$  states respectively.

### 2.3.1 Rate Equations

The rate equations describe a simple balance between the rate of change of total population of the levels involve and total number of laser photons.

The rate laws of the atoms population in  $i$  and  $k$  states are;

$$\frac{dN_i}{dt} = IP_i + N_k \Gamma_{ki} - N_i (\Gamma_i + I\sigma_i) \quad 2.3$$

$$\frac{dN_k}{dt} = IP_k - N_k (\Gamma_k + I\sigma_k) \quad 2.4$$

Where,  $\Gamma_k$  is the total decay rate including radiative decay. At the steady state with condition,  $\frac{dN_i}{dt} = \frac{dN_k}{dt} = 0$ , so equations (2.3) and (2.4) can be simplified to;

$$N_i = \frac{IP_i + n_k \Gamma_{ki}}{\Gamma_i + I\sigma_i} \quad 2.5$$

$$N_k = \frac{IP_k}{\Gamma_k + I\sigma_k} \quad 2.6$$

By laser excitation,  $\Delta N$  of the atoms is promoted from  $i$  to  $k$  state. At this instant ( $t = 0$ ), the population of both the states are

$$N_i(0) = N_i - \Delta N \quad 2.7$$

$$N_k(0) = N_k + \Delta N \quad 2.8$$

Equations (2.7) & (2.8) are the initial conditions for the general solution of the rate equations.

The OG signal of equation (2.1), arising from the change of the discharge current due to the electron collision ionization, can now be related to the change of population after optical excitation by

$$\Delta S(t) = \Delta S_i(t) + \Delta S_k(t) = \Delta N_i(t)I\sigma_i + \Delta N_k(t)I\sigma_k \quad 2.9$$

Therefore, the general solution of equations (2.3) and (2.4) take the form:

$$S(t) = ae^{-bt} + ce^{-dt} \quad 2.10$$

Where  $a$  and  $c$  are the amplitude whereas  $b$  and  $d$  are the decay rates for the two states involved in a transition;

$$a = I\sigma_k + \frac{I\sigma_i \Gamma_{ki}}{\Gamma_i + I\sigma_i - \Gamma_k - I\sigma_k} \quad 2.10a$$

$$b = \Gamma_k + I\sigma_k \quad 2.10b$$

$$-c = I\sigma_i + \frac{I\sigma_i\Gamma_{ki}}{\Gamma_i + I\sigma_i - \Gamma_k - I\sigma_k} \quad 2.10c$$

$$d = \Gamma_i + I\sigma_i \quad 2.10d$$

### 2.3.2 Instrumental Time Constant

The effect of instrumental response is crucial in determining the fast time region of the OG signal [27], which cannot be neglected if full understanding of the OG signal is desired. The fast time region details include the steepness of the rising edge, temporal position of the peak maximum and the peak intensity. The instrumental response becomes less significant as the OG signal evolves in the time domain. Including  $\tau$ , equation (2.10) becomes:

$$S(t) = \frac{a}{1-b\tau} \left[ e^{-bt} - e^{-\frac{t}{\tau}} \right] + \frac{c}{1-d\tau} \left[ e^{-dt} - e^{-\frac{t}{\tau}} \right] \quad 2.11$$

Here the parameters  $a$ ,  $b$ ,  $c$  and  $d$  have the same definitions as those in equation (2.10) and  $\tau$  is the instrumental time constant of the signal.

### 2.3.3 Effect of Discharge Current

In a gas discharge at a certain pressure and applied field, the collisional ionization regulates the current in the medium and for a given discharge parameters, a steady state current flows through the discharge. When the discharge is irradiated by a frequency, which corresponds to certain atomic, or molecular transitions of the gaseous species, a change in the steady state population of two or more states occur. As collisional ionization rates of different states are different, therefore change in the state population causes a change in the ionization balance of the discharge thereby causing a change in the steady state current of the discharge. In the present theoretical model, while solving the differential equations (2.3) and (2.4), we assume that the discharge current is constant. This should be a good approximation, because the relative change in the discharge current is very small [29]. It is predicted that with a certain discharge current change the

decay rates for the upper and lower states should be linearly related to the discharge current as given by equations.

$$b = \Gamma_k + I\sigma_k$$

and

$$d = \Gamma_i + I\sigma_i$$

Where as  $b$  and  $d$  are the decay rates for the two states involved in a particular transition.

# CHAPTER 3

---

## Experimental Setup

### 3.1 Introduction

The experimental setup to study the required optogalvanic spectra of Xenon is shown in figure (3.1). It consists of a dye laser pumped by a Nd-YAG laser system (Quanta Ray, GCR 11) and commercial hollow cathode lamps (Photron, Australia). The laser beam obtained from a dye laser was further divided into three parts by using beam splitters in its path. One part of the dye laser beam was directed to one of inert gas filled hollow cathode lamp through 1 *mm* diameter aperture. The second part was directed to other hollow cathode lamp, which produces well-distributed spectral lines, accurately known and listed in the M.I.T. Tables (1982), which have been used for the wavelength calibration. The third part was passed through a 2 *mm* thick solid etalon. These hollow cathode lamps were operated through a regulated DC power supply capable of delivering 200 *V* and 20 *mA* when a 10 *kΩ* load resistor was inserted in series with the hollow cathode lamp and a DC power supply. Time-resolved signals at constant laser energy were registered on a storage oscilloscope, the time-integrated signals at various current values ranging from 2 *mA* to 6 *mA* and the etalon rings were simultaneously recorded using the Boxcar Averagers (SR-250) and the data were stored on a PC through a General Purpose Interface Bus (GPIB) for subsequent analysis. While doing this experiment we made, use of different instruments, a brief introduction of each of which is given below.

### 3.2 Nd: YAG Laser (Pumping Source)

A pulsed laser system, Quanta-Ray GCR-11 was used to optically pump the dye lasers, which consists of an Nd: YAG laser, Harmonic Generator (HG) and Dichroic Mirrors (DHS). The HG generates the second and third harmonics while DHS is used to separate the second and third harmonics, 532 *nm* and 355 *nm* respectively.



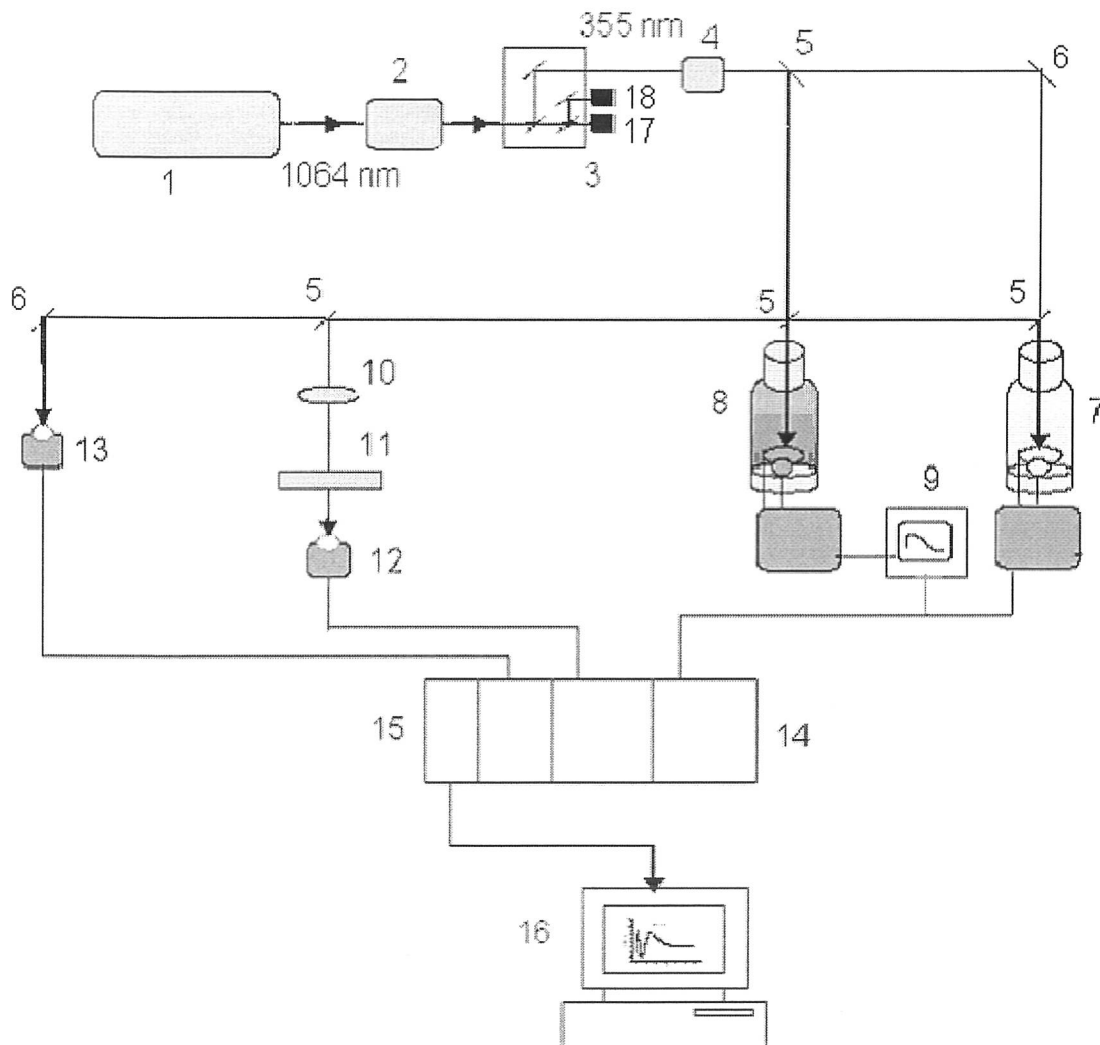


Fig. 3.1: Schematic diagram of the experimental setup.

- |                               |                              |                                 |
|-------------------------------|------------------------------|---------------------------------|
| 1. Nd: YAG Laser System       | 2. Harmonic Generator        | 3. Harmonic Separator           |
| 4. Dye Laser Cell             | 5. Beam Splitter             | 6. Reflector                    |
| 7. Hollow cathode (Xenon)     | 8. Hollow cathode (Neon)     | 9. Oscilloscope                 |
| 10. Spherical lens            | 11. Etalon                   | 12. Photodiode                  |
| 13. Photodiode for triggering | 14. Boxcar Averager (SR-250) | 15. Computer interface (SR-245) |
| 16. PC or recorder            | 17. Dump (1064 nm)           | 18. Dump (532 nm)               |

The neodymium-doped yttrium aluminum garnet (Nd: YAG) is most widely used solid state laser, in which the active medium is triply ionized neodymium ( $Nd^{+3}$ ) hosted by YAG, which is optically pumped by flash lamps. The Nd: YAG is a four level laser system as shown in figure below.

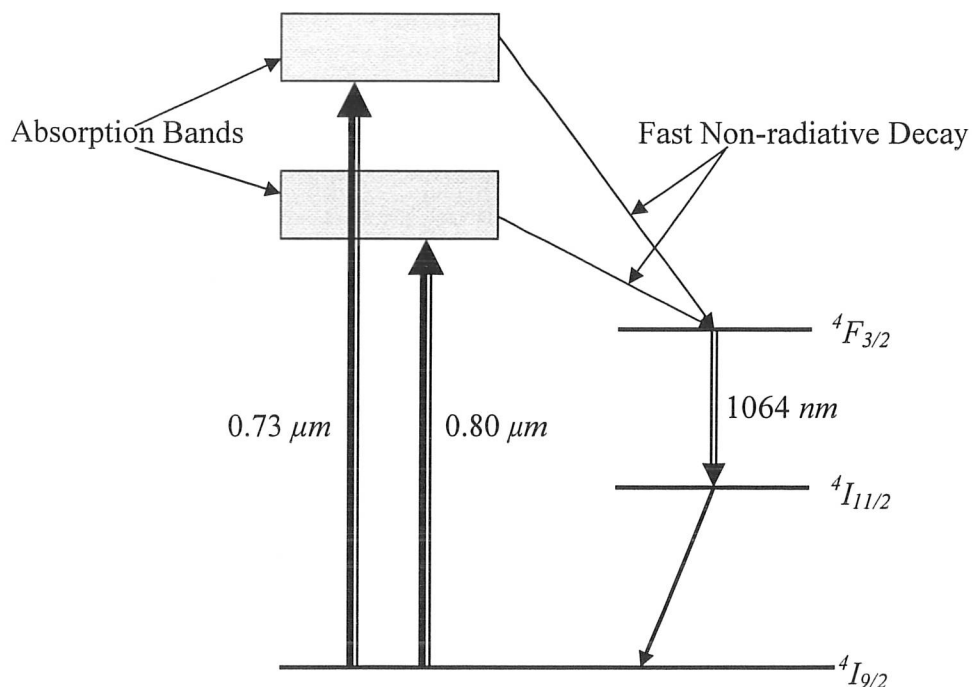


Fig: 3.2: Energy levels in Nd: YAG laser.

The flash lamps emit a broad spectrum of light, but the neodymium ions absorb most strongly at a limited range of wavelengths around  $0.7$  to  $0.8 \mu\text{m}$ . The absorbing photons in this range raises the neodymium ions from the ground state to the higher energy state, from where they decay to the  $^4F_{3/2}$  state, releasing their excess energy to the crystalline lattice. This state has comparatively long lifetime, about  $230 \mu\text{s}$ , hence this state will be populated heavily. In this state they are stimulated to emit  $1064 \text{ nm}$  laser transition dropping to a  $^4I_{11/2}$  laser level. The  $^4I_{11/2}$  is an unstable state, consequently the ions will rapidly return to the  $^4I_{9/2}$  ground state, producing a population inversion between the  $^4F_{3/2}$  and  $^4I_{11/2}$  states and thus the lasing. The neodymium laser can be arranged in series, in an oscillator-amplifier configuration to obtain more pulsed power than is available from a single laser oscillator. A Q-switch is used to reduce the pulse duration and to raise its peak power.

Harmonic Generator (HG) doubles or triples the fundamental frequency  $1064\text{ nm}$  and generates the second or third harmonic with wavelengths  $532\text{ nm}$  and  $355\text{ nm}$  by using a non-linear crystal with higher conversion efficiency called Potassium Dideuterium Phosphate (KD\*P) crystal. In our laser system pulse duration is from  $7\text{-}6\text{ ns}$ , and pulse energy of second harmonic is equal to  $135\text{ mJ}$ , where as the third harmonic pulse energy equals to  $60\text{ mJ}$ .

### 3.3 Dye Lasers

Dye lasers are classified as liquid lasers and are the most interesting type of lasers due to their significant properties. Dyes are organic, dissolvable in solvents like ethanol, methanol or water. The resultant solution follows dye's color.

Organic dye lasers were discovered in 1966 by Sorokin and Lankard [30] and Schäfer [31]. The first excitation of dye lasers was performed using pulsed ruby laser. This work was quickly followed by the successful demonstration of laser action using flash lamp pumping [32]. Dye laser action using the second harmonic of Nd: YAG laser was demonstrated in the same time period [33]. Flash lamp pumped dye lasers have been used to yield high energy pulses in the microsecond regime at a low pulsed repetition frequency (prf). Pulsed dye lasers are known to yield coherent tunable radiation at high average powers. An important feature of the laser dye as a liquid gain medium is its ability to flow at linear speeds, suitable for the necessary cooling. Flash lamp pumped dye lasers operating at a prf in the  $850\text{ Hz}$  range have been reported to yield up to  $1.2\text{ kW}$  in five second bursts [34]. A very important development was the introduction of the cw dye laser by Peterson [35]. This breakthrough provided the necessary infrastructure for the subsequent development of the femtosecond laser. The first narrow linewidth tunable laser oscillator was introduced by Hänsch in 1972 [36]. This telescopic Littrow grating configuration greatly enhanced intracavity dispersion by expanding the beam that illuminated the diffraction grating and line-width of about  $0.003\text{ nm}$  (at  $\lambda \sim 600\text{ nm}$ ) was achieved. Further narrowing in the line-width was achieved using an intracavity etalon [37]. About the same time Myers [38] and Stokes [39] reported the line-width less than  $0.1\text{ nm}$  using a single prism in the cavity (for the beam expansion). Hanna [40] reported the line-widths in the range of  $0.003\text{ nm}$  to  $0.007\text{ nm}$  by improving the single prism cavity

design. Using a grazing incidence angle, an alternate way of illuminating the grating was achieved by Shoshan [40] and Littman [41]. In this type of cavity, a line-width of the order of  $0.003 \text{ nm}$  at  $\lambda \sim 600 \text{ nm}$  was achieved.

However, there are two disadvantages in the use of single prism cavities as these employed the prism at a high angle of incidence, which causes significant optical power losses. Moreover, in the case of an open cavity the output is coupled with a high component of amplified spontaneous emission and the closed cavity leads to reduce efficiency. These shortcomings were tried to be overcome using multiple prism cavities. The generalized dispersion theory for multiple-prism arrays was introduced in 1982 by Duarte and Piper [42]. This theory is applicable to line-width narrowing and pulse compression. Tunable narrow line-width solid state dye lasers were demonstrated by Duarte in 1994 [43]. Work on crystalline laser dye gain media has also been the focus of recent research [44,45]. A significant advantage of solid-state gain media is that, once synthesis is perfected, its production costs are relatively low. The future of organic dye lasers is very bright. A wide range of industrial applications could benefit from the generation of cost effective tunable laser radiation in the visible region. Liquid, high average power dye lasers could make a significant contribution to the field, due to the discovery of new or modified highly stable water soluble dyes.

The selection of the dye and its concentration in the specific solvent depends on the wavelength required for the excitation scheme of the experiment. In the present work, we have recorded the optogalvanic spectra both integrated and time-resolved, produced by scanning the wavelength across the inert gases transitions.

### 3.3.1 Resonant Cavity

We have used the Hanna type dye lasers cavity in our experiments, as shown in figure (3.3). A holographic grating having  $2400 \text{ lines/mm}$  was coupled to a stepper motor. In a single step, motor covers approximately  $0.095 \text{ cm}^{-1}$  ( $0.002 \text{ nm}$ ) at  $400 \text{ nm}$ . In this cavity, a cylindrical lens focuses the pump laser into a horizontal line inside the dye cell, near its front surface. Due to the high gain of the laser dyes, a fluorescence spot from both sides of the dye cell is produced. On one side of the dye cell a 100% reflecting mirror reflects the fluorescence back into the cell. As a result we get a bright fluorescence on the other

side of the cell which then hits the prism at the grazing incidence. The prism then expands the fluorescence so that it covers the maximum grooves of diffraction grating for better resolution and narrow laser line-width. The diffraction grating reflects the fluorescence into cell through the prism. The mirror and the grating define the cavity of the laser. The wavelength tuning was achieved by rotating the grating by a computer controlled stepping motor.

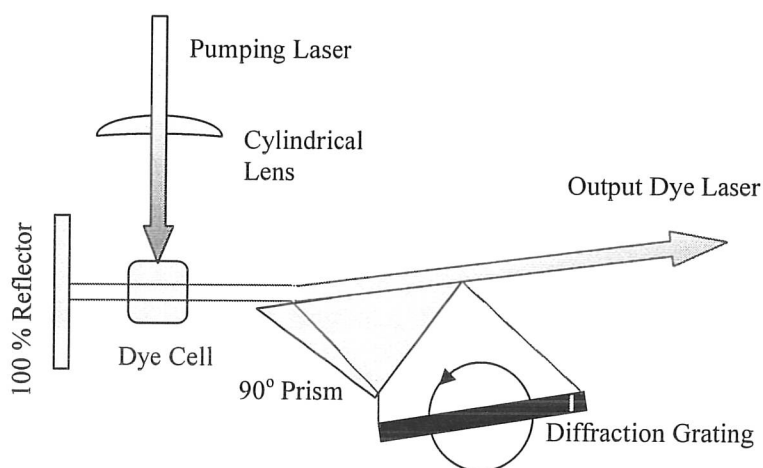


Fig: 3.3: A Hanna type dye laser.

### 3.3.2 Molecular Transitions and Spectra

The energy level diagram for a typical molecule is shown in figure (3.4). The ground states of most of the molecules are singlet, so that the absorption of light produces excited singlet states. Spontaneous emission then results in fluorescence. However, it is possible through a process called intersystem crossing for molecules to switch into their excited triplet states. Spontaneous emission from a triplet state occurs very slowly, by comparison with the fluorescent transitions, and is called phosphorescence. Molecular fluorescence is responsible for the dye laser emission. The range of the fluorescence wavelengths limits the wavelength of the laser emission. To choose a particular wavelength, we pick a dye with its fluorescence emission spectrum around the desired

laser wavelength. We must also choose a dye with a long-lived first excited singlet state, so that a population inversion is easy to build up. The dye should also be easily excited by the available light sources.

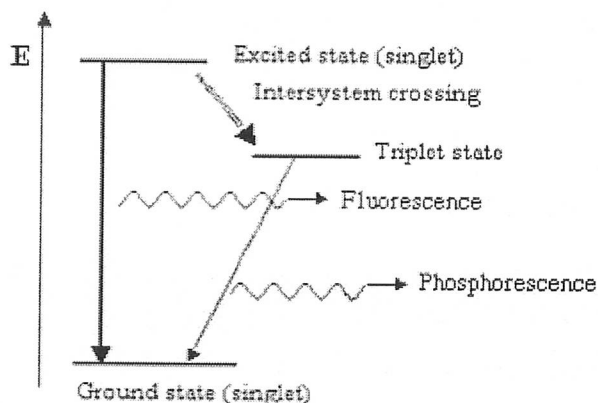


Fig: 3.4: Energy level diagram for molecular transitions.

### 3.4 Hollow Cathode Lamp

Hollow cathode lamp is a type of discharge lamp that produces narrow emission from atomic species. They are used to study the laser optogalvanic effects. It gets its name from the cup-shaped cathode, which is made from the refractory elements such as U, Sr, Ba, Cu, Fe, and Al etc. On the upper side of the cup-shaped cathode just a few *mm* away, there is a metallic ring known as anode. The operational current lies in the range of 5-10 *mA*. In order to get the maximum signal, the current favoring the optimum conditions is applied.

For our experiment we have used commercial hollow cathode lamps (Photron, Australia) filled with Xenon gas at a pressure of about 1 *torr*. Operating current for this hollow cathode lamp is 2 *mA* to 6 *mA*. In figure (3.5) geometrical construction of hollow cathode lamp is shown.

#### 3.4.1. Limitations of Hollow Cathode Lamp

- ❖ The main limitation of a hollow cathode lamp is that only one element can be analyzed at a time and we need changing the lamp for the analysis of the other element.

- ❖ Another problem, which is faced with the hollow cathode lamp, is the problem of self-absorption. This problem arises due to the diffusion of metal atoms of the cathode in the sample being analyzed. This problem can be avoided by running the lamp at a low current value.
- ❖ When the lamp remains in use for a sufficiently long time, the metal atoms deposit on the walls of the lamp. The deposition of metal atoms on the lamp window reduces the lamp intensity. This can be avoided by separating the cathode and the window regions of the lamp.

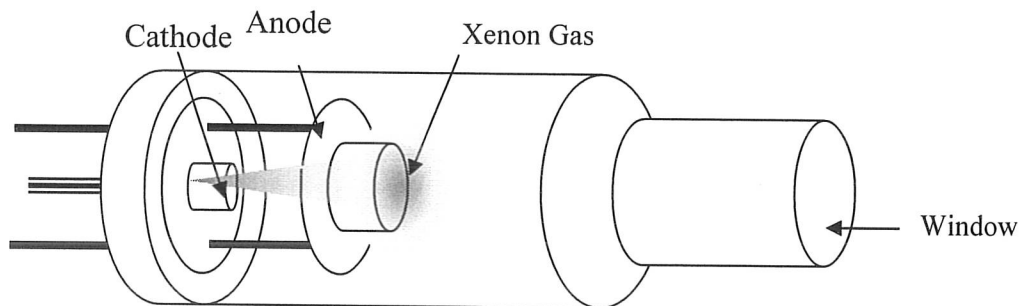


**Fig: 3.5:** Xenon filled hollow cathode lamp.

### 3.5 Fabry-Perot Etalon

In 1889 Charles Fabry and Alfred Perot designed a device called “Fabry-Perot Etalon”, which brought about a significant improvement in Michelson Interferometer. It works in a similar way as a resonant cavity in laser.

Etalon is used as a standard of length calibrated in terms of the wavelength of spectral lines. This instrument is shown in figure (3.6), is used to produce circular, sharply defined interference fringes from the light from an extended source. The rings on the screen are images of those points on the source producing light going in suitable directions between the lenses. In etalon the central cavity is usually made of two glass plates, with their inner surfaces coated with partially transparent films of high reflectivity. These plates are held apart by an optically worked spacer made of silica to which they are pressed by springs.

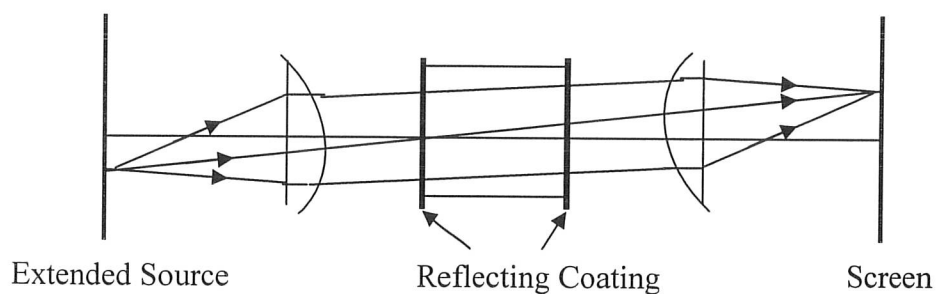


Fig: 3.6: A Fabry-Perot Etalon.

### 3.6 Photodiode

Photodiodes are doped semiconductors, which are used as photovoltaic or photoconductive devices. When the pn-junction of the diode is irradiated, the photo voltage is generated across the diode; with in a restricted range it is proportional to the absorbed radiation. Diode used as photoconductive elements change their internal resistance upon irradiation and therefore can be used as photo resistors in combination with an external voltage source. In the present experiment the laser pulse through a photodiode triggered both the oscilloscope and the Boxcar Averager System.

### 3.7 Data Acquisition System

The laser optogalvanic technique possesses a high signal to noise ratio. The best method to recover a signal from accompanying noise depends very much on the nature of the signal in question and the required representation of the result. There are some techniques to improve the signal to noise ratio and to transform the signal to a desired format. Some instruments are developed which can help to optimize the measuring procedure, which are explained below:

#### 3.7.1 Boxcar Averager

We used the Boxcar averager to acquire and analyze the recovered fast analog signals. We used the SR-250 boxcar (Stanford Research Systems) which is a versatile, high speed, and designed to recover fast repetitive fast analog signals. It consists of a gate



generator, a fast gated integrator, and the exponential averaging circuitry. The gate generator can be triggered internally or externally and provides an adjustable delay from a few nanoseconds to 100 milliseconds. The SR-250 is a complete, single channel gated integrator and box car averager with gate widths from 2 ns to 15  $\mu$ s. The boxcar averager uses an analog electronics, supported by digital control, to monitor one discrete point in time on a repetitive signal. It builds up an average of that point over many cycles before recording it as a value; it may then move to a different value and repeat the same process. In this way it can step across a waveform which is a complete averaged representation of the input signal. In our case the gate generator is triggered externally by the Nd-YAG laser. Using an oscilloscope (triggered externally from the same source) and the front panel of the potentiometer the gate position is adjusted to sample only the peak of the signal. The fast gated integrator amplifies and integrates the input signal during the time when gate is open. In SR-250 we can average from 1 to 10,000 samples. Average of many noisy signals converges to the mean value of the signal as the random noise averages almost to zero.

### 3.7.2 Oscilloscope

An oscilloscope is used for producing a visual image of one or more rapidly varying electrical quantities. A four channel oscilloscope (Tektronix TDS-2024) was used to view the signal shape and to measure voltage of the pulse generated due to ionization in HCL. It was also triggered externally with the help of a photodiode by shining a small portion of laser light it. It was also used to trigger the gate at the maximum point of signal and to optimize the signal

### 3.7.3 PC Recorder

A PC connected to Boxcar Averager through GPIB Card was used for storing and processing the information received in a prescribed and acceptable form according to asset of instruction. An IBM PC-486 was used to run the dye laser motor (stepper motor) which moves/rotates the grating in regular steps, and to record the signal from the second/ionizing dye laser, Xenon discharge cell (HCL), and from the photodiode implied

to show the diffraction signals formed by the etalon. The data was stored after each experimental run for further analysis.

# CHAPTER 4

---

## Results and Discussions

### Summary

In this chapter, we study the dominant physical processes responsible for the production of the optogalvanic signal in the spectra of Xenon. Time-resolved spectra are obtained at a fixed wavelength of the dye laser resonantly tuned to an optically allowed transition. The temporal evolutions of the signals are registered on a storage oscilloscope. Two transitions from the  $6s[3/2]_2$  metastable and one from  $6s[3/2]_1$  state corresponding to  $\Delta J = \Delta K = 0, \pm 1$  dipole selection rules, have been selected to investigate the dominant physical processes responsible for the optogalvanic signals. The change in the signal amplitude as a function of the discharge current has been registered. In addition the electron collisional ionization rate parameter ratios have been determined for the transitions corresponding to the dipole selection rules,  $\Delta J = -1 \Delta K = 0$ ,  $\Delta J = 1 \Delta K = 0$  and  $\Delta J = \Delta K = 0$  as 23, 1.2 and 12.4 respectively. The effective lifetimes of the upper levels involved in the previously mentioned transitions are also calculated as 0.33  $\mu s$ , 0.28  $\mu s$  and 0.06  $\mu s$  respectively.

### 4.1 Introduction

In a gas discharge, at a certain pressure and applied field, the collisional ionization regulates the current in the medium and for a given discharge parameters, a steady state current flows through the discharge. Such a steady state can be disturbed by a resonant radiation that results in a change of population distribution of energy levels. Since the collisional ionization rates of different levels are different, so a change in level population causes a change in the ionization balance of the discharge. The atom's long lived metastable levels, by colliding with high energy electrons or by means of metastable-metastable collisions, play a very important role in the ionization processes.

In the theoretical model, that is rate equation model, discussed in chapter 2, it was predicted that with in a certain range of discharge current the decay rates for the upper and lower levels should be linearly related to the discharge current. On the basis of this prediction, in the present chapter, we identify which dominant physical phenomenon is responsible for the optogalvanic signal in the spectra of Xenon. The experimental setups, to study the time-resolved optogalvanic spectra have been described in chapter 3.

## 4.2 Energy Levels

The ground state electronic configuration of rare gases, excluding helium, is  $mp^6\ ^1S_0$ , where  $m = 2, 3, 4$  and  $5$  for Neon, Argon, Krypton and Xenon respectively. The excited levels of these gases are best described by the  $j_cK$  coupling scheme [3,4]. According to this scheme, the first group of the excited levels above the ground state has a  $mp^5(m+1)s$  configuration. This results in four energy levels namely,  $mp^5(m+1)s\ [3/2]_2$ ,  $mp^5(m+1)s\ [3/2]_1$ ,  $mp^5(m+1)s'\ [1/2]_0$  and  $mp^5(m+1)s'\ [1/2]_1$ . Two of these levels  $mp^5(m+1)s\ [3/2]_2$  and  $mp^5(m+1)s'\ [1/2]_0$  are metastable levels. One, the  $mp^5(m+1)s\ [3/2]_1$ , is semi-metastable, while the  $mp^5(m+1)s'\ [1/2]_1$  is short lived and is termed as resonance level. The metastable levels, as they are not connected to the ground state by means of electric dipole transition ( $\Delta J = 0, \pm 1$ ; excluding 0-0), have radiative lifetimes of the order of seconds, whereas, for the other two levels this time is of the order of ns. Similarly, the second group of excited levels come from the  $mp^5(m+1)p$  configuration. This results in 10 energy levels.

Under this scheme the first excited state for Xenon  $5p^56s$  gives rise to four levels namely  $6s[3/2]_2$ ,  $6s[3/2]_1$ ,  $6s[1/2']_0$  and  $6s[1/2']_1$ . Here prime refers to the terms generated from the  $5p^5\ ^2P_{1/2}$  parent ion level. The  $6s[3/2]_2$  and  $6s[1/2']_0$  levels are metastable, with radiative life times,  $149.5\ s$  and  $0.078\ s$  [46], while the other two levels  $5p^56s[3/2]_1$  and  $5p^56s[1/2']_1$  have radiative life times of the order of few seconds. The second group of excited states arises from the  $5p^56p$  configuration that reveals ten energy levels designated by  $6p[3/2]_2$ ,  $6p[3/2]_1$ ,  $6p[1/2']_1$ ,  $6p[1/2']_0$ ,  $6p[5/2]_3$ ,  $6p[5/2]_2$ ,  $6p[3/2]_2$ ,  $6p[3/2]_1$ ,  $6p[1/2]_1$  and  $6p[1/2]_0$ .

## 4.2.1 Time-Resolved Optogalvanic Spectroscopy

The time-resolved optogalvanic spectrum has been obtained at a fixed dye laser wavelength tuned in resonance with a dipole allowed electronic transition. The time-resolved signals are taken directly from the oscilloscope. In order to understand the collisional ionization of the excited states of Xenon atoms in gas discharge plasma, we selected three cases of Xenon transitions. A schematic energy level diagram and relevant transitions are shown in figure (4.1). The solid lines in the figure represent the one-photon excitation that gives rise to the optogalvanic signal whereas the dotted lines represent possible decay paths within the framework of the  $j_c K$  coupling scheme.

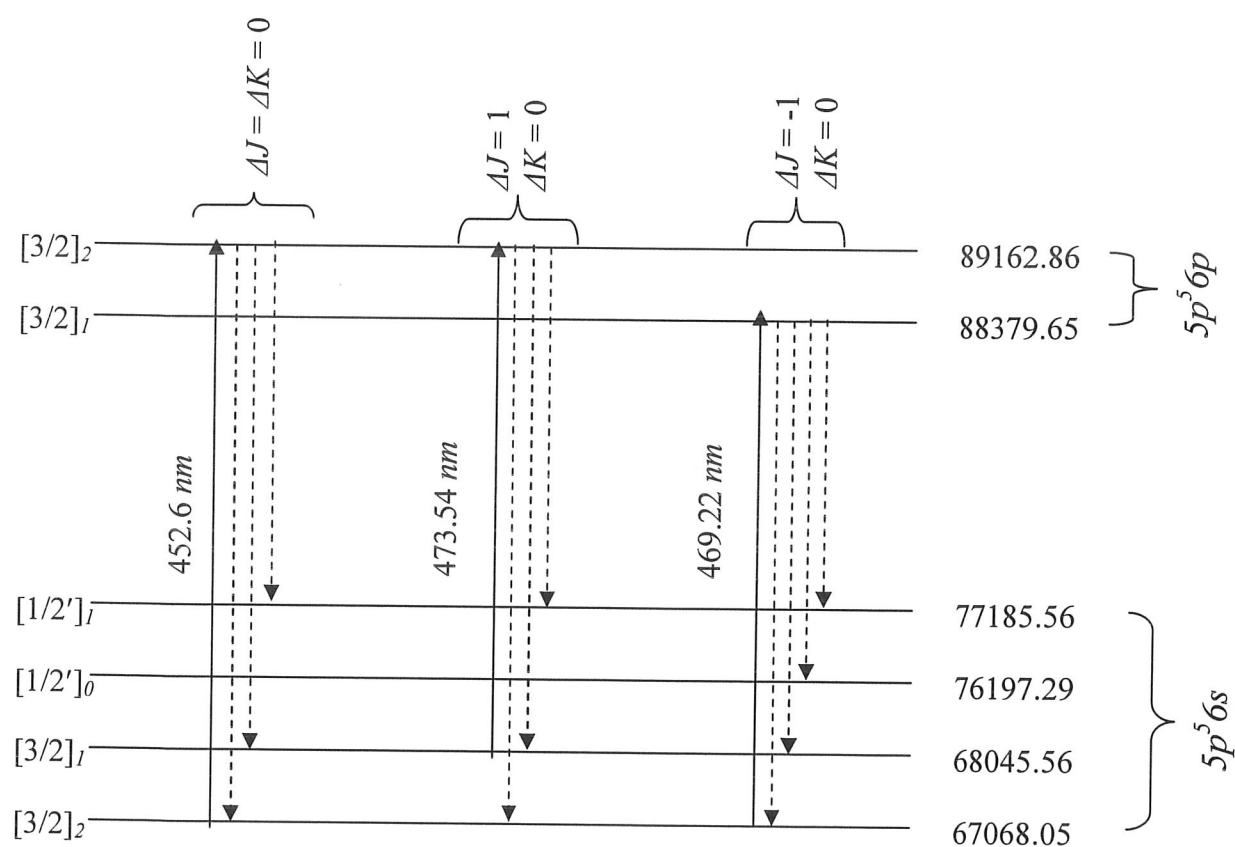


Fig: 4.1 Partial energy level diagram for Xenon transitions.

The laser optogalvanic signal can be either positive or negative, composed of a fast rising peak followed by an exponential decay to the signal with an opposite sign, which then

returns to the base line. We have used a least square program to fit the observed time-resolved signals to the equation

$$S(t) = \frac{a}{1 - b\tau} \left[ e^{-bt} - e^{-\frac{t}{\tau}} \right] + \frac{c}{1 - d\tau} \left[ e^{-dt} - e^{-\frac{t}{\tau}} \right] \quad 4.1$$

and determined the amplitudes and decay rates of the previously mentioned transitions. This expression reproduces the experimentally obtained time-resolved optogalvanic signal with only five parameters.

A typical time resolved optogalvanic signal curve is shown in figure (4.2). Two deconvoluted exponential components of equation (4.1) are also shown in figure (4.2), each representing decays of Xenon population in one of the energy state involved in optical excitation. We first fitted the exponential decays to obtain the initial values of the decay rates before fitting the complete curve. At the end, the instrumental response time was also added in the fitting procedure.

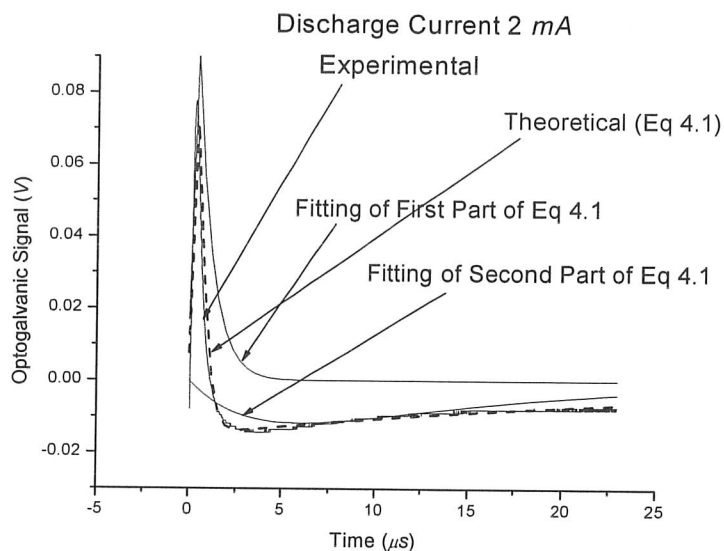


**Fig: 4.2** Observed and fitted optogalvanic signal at 2 mA discharge current of two deconvoluted signals represent the positive and negative exponential components of equation (4.1).

### 4.3 Experimental Results

Here we present the results we have obtained, these can be classified into:

- ❖  $\Delta J = -1 \quad \Delta K = 0$
- ❖  $\Delta J = 1 \quad \Delta K = 0$
- ❖  $\Delta J = \Delta K = 0$

#### 4.3.1 Case-1 ( $\Delta J = -1, \Delta K = 0$ )

We have chosen the  $5p^56s[3/2]_2 \rightarrow 5p^56p[3/2]_1$  transition to study the collisional ionization of the excited state in the Xenon discharge plasma. The wavelength required for this transition is  $469.22 \text{ nm}$ , it was achieved by using the dye C-460 dissolved in methanol. Figure (4.3) shows the observed time-resolved optogalvanic signal, the fitted curve is also shown with solid line. This particular data was taken at a current of  $2 \text{ mA}$ .

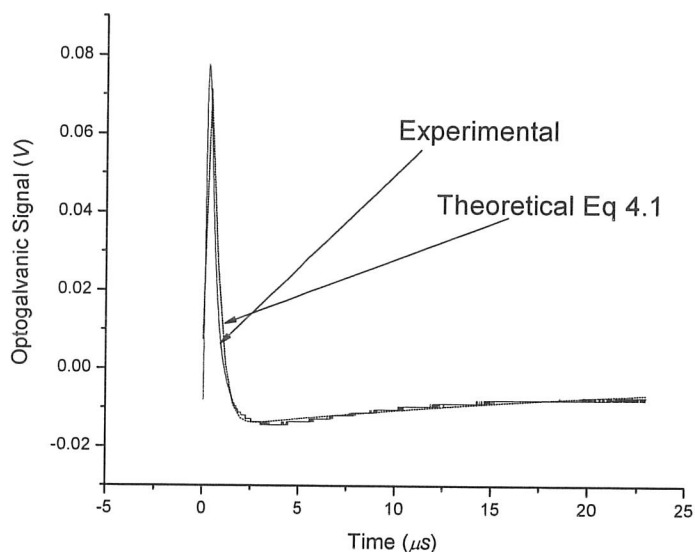


**Fig: 4.3** Time-resolved optogalvanic signals of Xenon at  $469.22 \text{ nm}$  following the  $\Delta J = -1, \Delta K = 0$  selection rules. (a) Dotted line, which passes through the observed data points is the least square fit to equation (4.1). The signal was recorded at  $2 \text{ mA}$  discharge current.

By changing the discharge current from  $2 \text{ mA}$  to  $6 \text{ mA}$ , a set of time-resolved optogalvanic signals is compiled to study the effect of the discharge current. We have

selected this current range because if the current is less than the optimized value the discharge was not stable. The upper limit of the current was set because signal above that value were found to be saturated. These traces are shown in figure (4.4). The optogalvanic signals consist of fast rising peaks followed by decay to the negative side and then signal getting back to the base line level. Each spectrum shows a least square fit of the theoretical model (Eq. 2.11) to the observed data of the time-resolved signal. The laser energy at each trace was kept constant. The decay rates depend on the discharge current of the lamp i.e. higher current produces faster decay (see table 4.1) and smaller peak amplitudes. With the increase of the discharge current the probability of ionization of the upper level  $6p[3/2]_l$  increases. Because of the large ionization cross-section of the upper level an increase in its population results in higher ionization rates. This is because it causes both an increase in the number density of atoms in the upper level and a change in the electron distribution function [48]. Thus the current will increase with the corresponding voltage decrease across the discharge to maintain the steady state condition. As a result, the optogalvanic signal will decrease in magnitude.

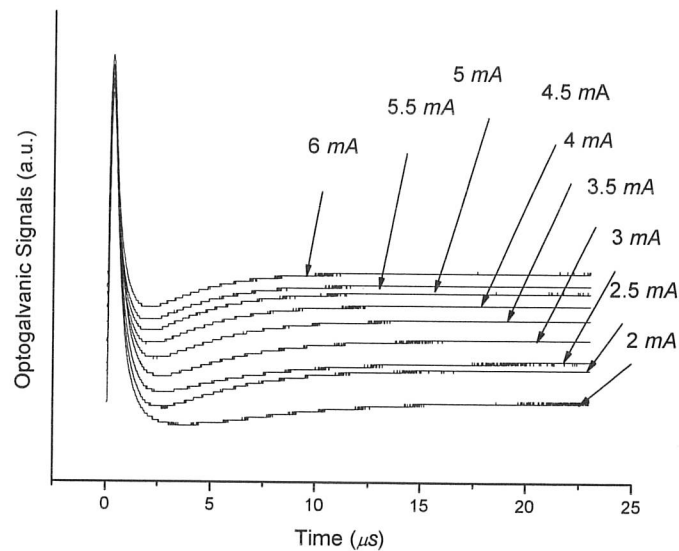


**Fig: 4.4** Set of time-resolved optogalvanic signals registered at different discharge currents.

The variation of signal amplitude as a function of discharge current is shown in figure (4.5). From the plot it is evident that the variation of the signal amplitude as a function of



current obeys an exponential law as expected with the diffusive motion of electrons in the discharge plasma.

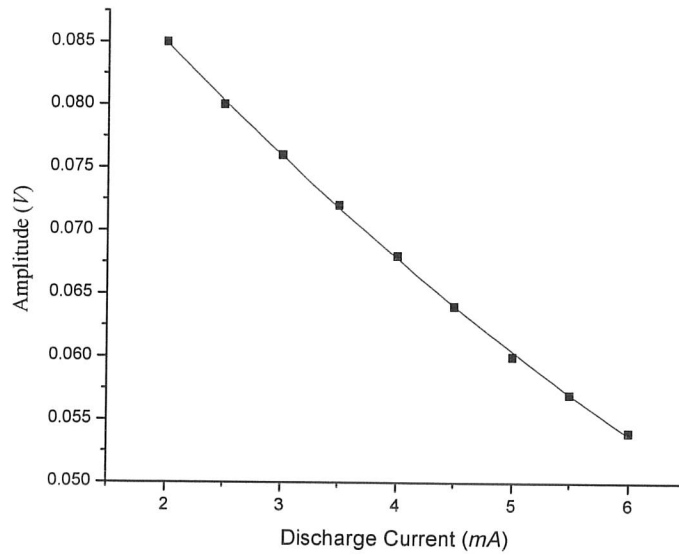


**Fig: 4.5** Plot of the optogalvanic signal amplitude vs discharge current. The signal decreases with the increase of the discharge current.

The decay rates using theoretical rate equation model are defined by

$$b = \Gamma_k + I\sigma_k \quad 4.2$$

and

$$d = \Gamma_i + I\sigma_i \quad 4.3$$

Here  $b$  and  $d$  are the decay rates,  $\sigma_i$  and  $\sigma_k$  the electron collisional ionization rate parameters and  $\Gamma_k$  and  $\Gamma_i$  the effective decay rates of the upper and lower levels respectively.

The decay rates plots verses discharge current are shown in figure (4.6). It is noticed that within a certain discharge current range, the  $b$  and  $d$  values are linearly related to the discharge current as it is predicted in the theoretical model. The observed data points are represented by the following parameters obtained by a linear regression fitting:

$$b = 3.06 + 0.23 I \quad 4.4$$

$$d = 0.01 + 0.01 I \quad 4.5$$

Here  $b$  and  $d$  are in ( $\mu s^{-1}$ ) and the discharge current  $I$  in  $mA$ . The experimental values of  $b$  and  $d$  are comparable with the theoretical predications of equations (2.10b) and (2.10d). However it is difficult to compare the experimental values of  $a$  and  $c$  because these two

parameters are highly correlated with each other so the fit does not yield unique values for  $a$  and  $c$ . This correlation does not affect the  $b$  and  $d$  values.

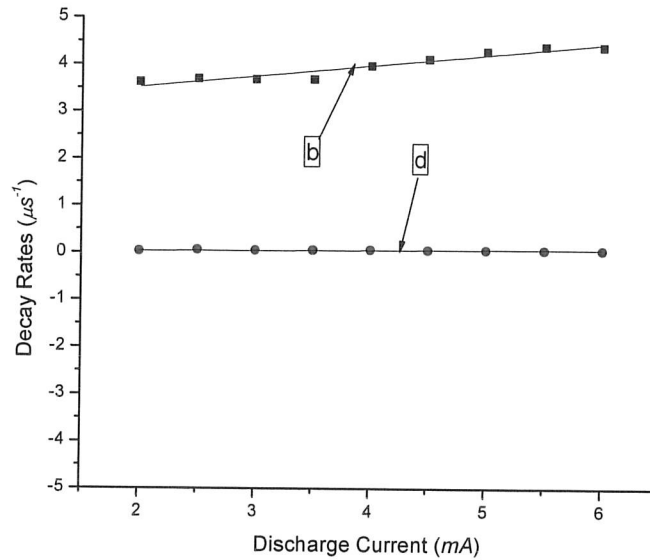


**Fig: 4.6** Plot of the decay rates vs the discharge current. Solid lines are the least square fits to equations (4.2) and (4.3).

The values of these constants are given in Table 4.1. The amplitude of the positive peaks are also shown in this table. After comparing the theoretical decay rates (Eq: 4.2 & Eq: 4.3) and observed decay rates (Eq: 4.4 & Eq: 4.5), some important conclusions have been drawn.

#### 4.3.1a Lengthening of the Effective Life Time of the Upper Level

The effective decay rate of the upper level  $\Gamma_k = 3.06 \mu s^{-1}$  gives the effective lifetime of this state to be  $\tau_k = 0.33 \mu s$ . The radiative lifetime of the  $6p[3/2]_1$  level is  $28.7 ns$  [48]. The possible mechanism for this lengthening is attributed to radiation trapping. The radiation trapping can be explained as follows: when atoms are excited the by resonance radiation the resulting fluorescence from the volume occupied by the atoms may be delayed due to subsequent re-absorption & emission of the original fluorescent quanta. In the present case the upper level  $5p^5 6p[3/2]_1$  is optically connected to the resonance levels  $5p^5 6s[3/2]_1$  and  $5p^5 6s[1/2]_1$  as well to the metastable levels  $6s[3/2]_2$  and  $3s[1/2]_0$ .

The radiation trapping occurs during the de-excitation of these resonance levels in the discharge tube. This process is unique because the resonant radiation turns out to be trapped in the discharge tube. The emitted photon is absorbed by another atom so that the effective lifetime of the excitation within the system greatly exceeds the radiative lifetime of a level. Metastable state population plays an important role in the ion production in a discharge tube. Through collisions and tube wall losses its population is depleted. Stewart, Mcknight and Hamad [28] calculated the tube wall losses, metastable densities, branching ratio and escape factor  $g$ . They used the expression for the escape factor given by Fujimoto [49];

$$g = \frac{1 - k_0 r}{0.86 + k_0 r}$$

In this expression  $k_0 r$  is the optical thickness at the line center and  $r$  is the cylindrical radius. Due to limitations of our theoretical model and little information available about the commercial hollow cathode lamp we cannot relate imprisonment factor to our extracted values of the effective lifetimes. On the basis of the previous work we may speculate that the lengthening of the effective lifetime of the upper level is due to radiation trapping.

#### 4.3.1b Effective Electron Collisional Ionization Rate Parameter

The extracted electron collisional ionization rate parameters for the upper and lower levels are  $\sigma_k = 0.23 \text{ mA}^{-1} \mu\text{s}^{-1}$  and  $\sigma_i = 0.01 \text{ mA}^{-1} \mu\text{s}^{-1}$  respectively. The effective electron collisional ionization rate parameter of the upper level is larger than that of the lower level. The ratio of these two parameters ( $\sigma_k/\sigma_i$ ) is 23, which is proportional to the total ionization cross-sections. However, the determination of the absolute magnitude of the cross-sections requires more experimental information. Since the upper level  $5p^5 6p[3/2]_1$  has a larger ionization rate parameter therefore its population is increased because the ionization depends strongly on the population distribution of various levels. On the basis of the ratio of the electron collisional ionization rate parameters ( $\sigma_k/\sigma_i$ ) extracted in the present work, it is concluded that the electron collisional ionization is the dominant physical process contributing to the generation of the optogalvanic signal in the Xenon hollow cathode discharge.

4.3.2 Case-2 ( $\Delta J = 1, \Delta K = 0$ )

The transition  $5p^56s[3/2]_1 \rightarrow 5p^56p[3/2]_2$  at 473.54 nm obeying the above mentioned selection rule is chosen to study the time-resolved optogalvanic signal. This wavelength was achieved by using the C-460 dye dissolved in methanol. One of the trace, recorded at 3.5 mA is shown in figure (4.7), this figure also shows the result of the least squares fit to equation (4.1). In figure (4.8) we have shown the various traces recorded at different current values ranging from 2 mA to 5.5 mA. The dye laser energy is kept constant in all these traces. As observed earlier, each optogalvanic signal comprises first a fast rising peak followed by an exponential decay of signal with opposite sign and in the end converging back to the base line. The signal intensity decreases with current and is plotted in figure (4.10).

The importance of collisions in the discharge plasma can be understood by comparing the collisional rates with the radiative rates. When the collisional rates dominate the radiative rates, the excess population of the  $5p^56p[3/2]_2$  level is transferred to the other  $5p^56p$  configuration-based levels and consequently the atoms will quickly decay back to the  $5p^56s$  configuration-based levels. The high collisional rates then quickly mix the population in the  $5p^56s$  levels achieving a steady state value and the optogalvanic signal disappears. Since we have observed the optogalvanic signals on the microsecond time-scale, therefore the effective lifetime of the  $5p^56p[3/2]_2$  must be of the order of microseconds.

In this case the decay rates are also linearly related to the discharge current as has been observed in case-1. The results of fitting  $b$  and  $d$  to equation (4.2 and 4.3) over the range of the discharge current (2 mA to 5.5 mA) are plotted in figure (4.9). This figure clearly shows that the effective collision decay rate  $d$ -parameter follows a linear dependence.

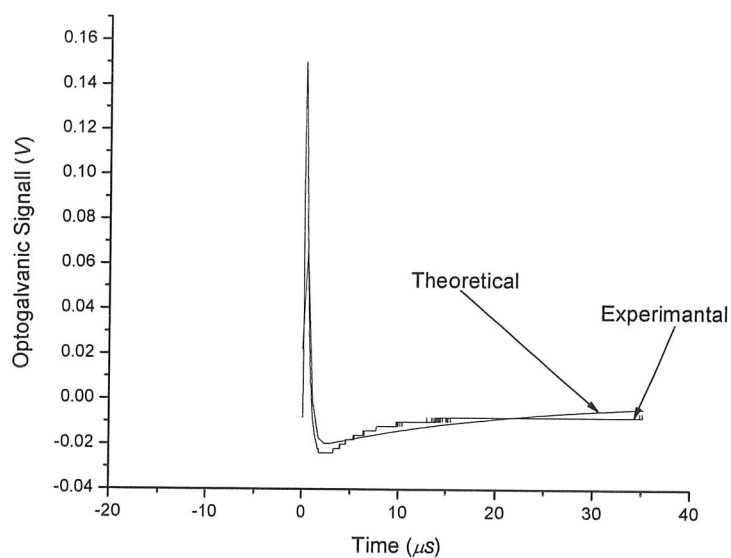


**Fig: 4.7** Time-resolved optogalvanic signals of Xenon at 473.54 nm corresponding to  $\Delta J = 1$ ,  $\Delta K = 0$  selection rules. The signal was registered at 3.5 mA discharge current.

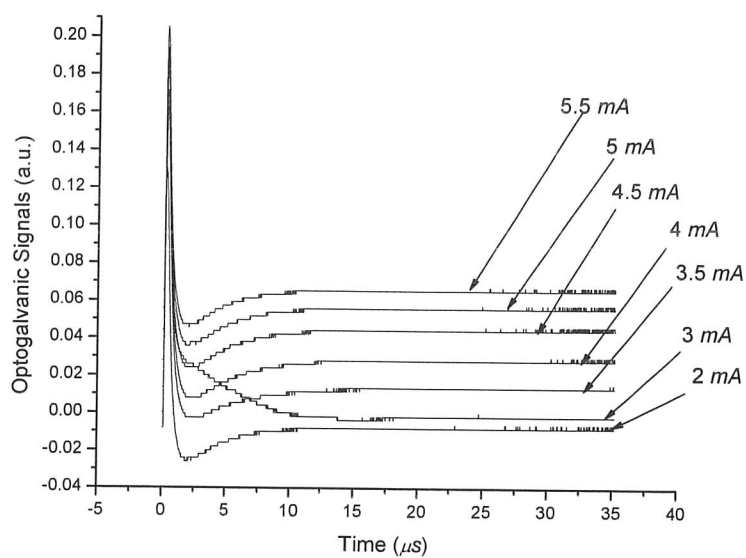


**Fig: 4.8** Set of time-resolved optogalvanic signals compiled at different discharge currents ranging from 2 mA to 5.5 mA.

The data points in the linear regression are represented by the following relations.

$$b = 3.58 + 0.06 I \quad 4.6$$

$$d = 0.28 + (-0.05) I \quad 4.7$$

Comparing these equations with Eq: (4.2 & 4.3), the effective decay rates of both the levels following the laser excitation are  $\Gamma_k = 3.58 \mu s^{-1}$  for the upper level and  $\Gamma_i = 0.28 \mu s^{-1}$  for the lower level.

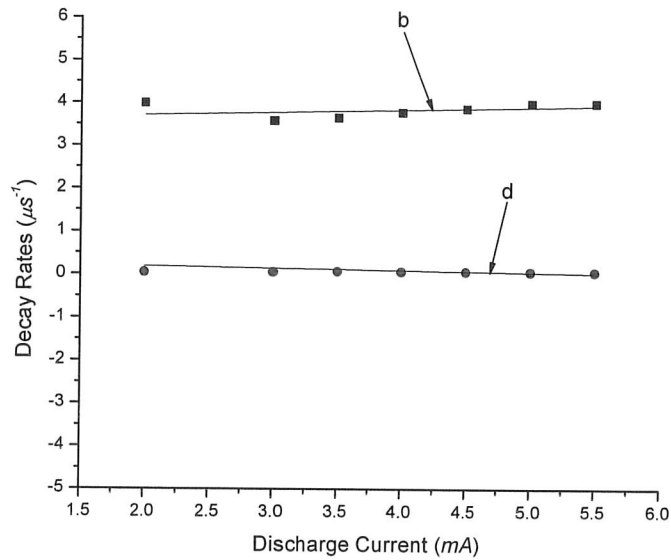


**Fig: 4.9** Plot of decay rates vs discharge current for Xenon 473.54 nm. The solid lines, which pass through the observed data points, are the least square fits to equations (4.2) and (4.3).

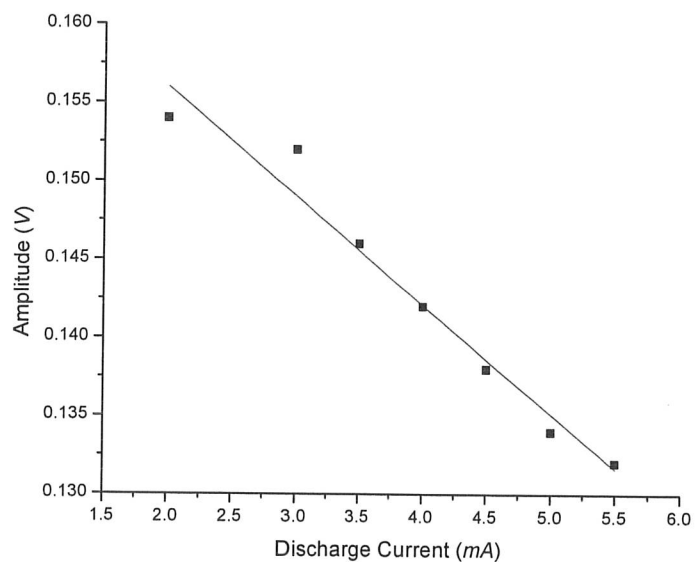


**Fig: 4.10** Plot of the signal amplitude vs discharge current for Xenon 473.54 nm. The signal decreases with the increase of the discharge current.

The effective lifetime for the upper level is  $0.28 \mu s$ , which is longer than the radiative lifetime, which is  $28 ns$  [48]. The corresponding collisional ionization rate parameters are  $\sigma_k = 0.06 mA^{-1} \mu s^{-1}$  and  $\sigma_i = -0.05 mA^{-1} \mu s^{-1}$ , respectively. The ratio of these two parameters ( $\sigma_k/\sigma_i$ ) is 1.2. It shows that in this case again the electron collision ionization is the dominant physical process responsible for the production of the optogalvanic signal. In table (4.2) the fitted parameters and the amplitudes at different discharge currents are presented.

#### 4.3.3 Case-3 ( $\Delta J = \Delta K = 0$ )

For this case we have chosen the  $5p^56s[3/2]_2 \rightarrow 5p^56p[3/2]_2$  transition at  $452.6 nm$ . We recorded the Optogalvanic signal at different discharge currents, while in each case laser energy is kept constant. In figure (4.11) one of the trace recorded at  $2 mA$  is shown along with the fitted curve. All the recorded traces in the current range  $2.5 mA$  to  $6 mA$  are shown in figure (4.12). This figure (4.12) shows that with increasing discharge current the signal intensity almost remain constant. A possible explanation for this is that the population is again distributed to the levels where ionization probability is high. The change of metastable concentration as a function of discharge current is plotted in figure (4.14).

The decay rates are also linearly related to the discharge current. From the plot of decay rates vs discharge current (Fig 4.13), we conclude that the effective lifetime of the  $5p^56p[3/2]_2$  level is  $0.06 \mu s$ , which is longer than its radiative lifetime,  $28 ns$  [48]. The extracted collisional rate parameters for the upper and lower levels are  $\sigma_k = 1.74 mA^{-1} \mu s^{-1}$  and  $\sigma_i = 0.14 mA^{-1} \mu s^{-1}$  respectively. The ratio of these parameters ( $\sigma_k/\sigma_i$ ) is equal to 12.4, which reveals again that the electron collisional ionization, responsible for the optogalvanic signal. In table (4.3) the fitted parameters and amplitudes at different discharge currents are presented.

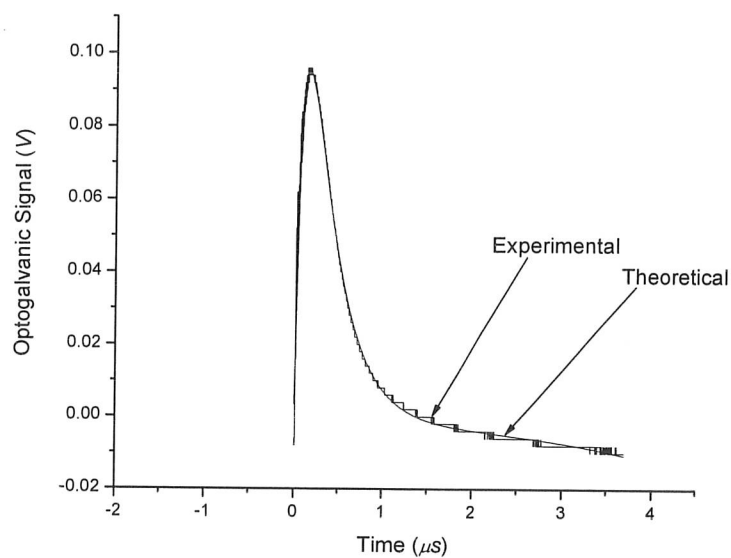


**Fig: 4.11** Time-resolved optogalvanic signals of Xenon at 452.6 nm corresponding to  $\Delta J = \Delta K = 0$  selection rules. The signal was registered at 2 mA discharge current.

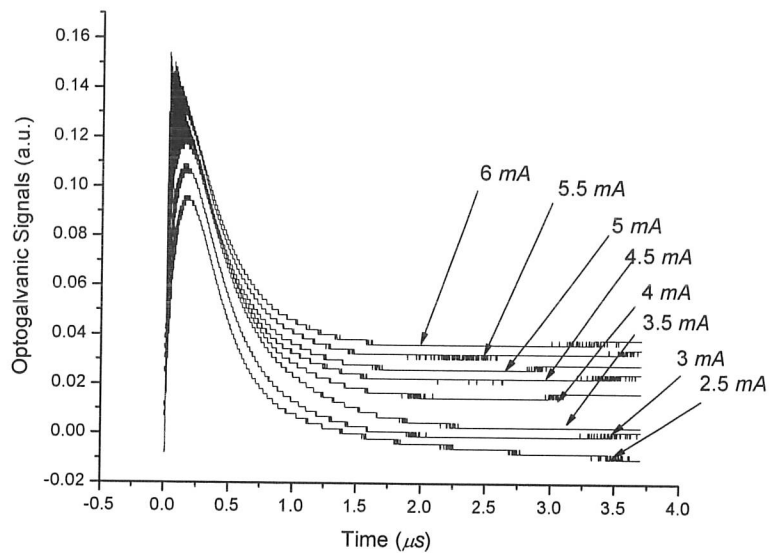


**Fig: 4.12** Set of time-resolved optogalvanic signals compiled at different discharge currents ranging from 2.5 mA to 6 mA.



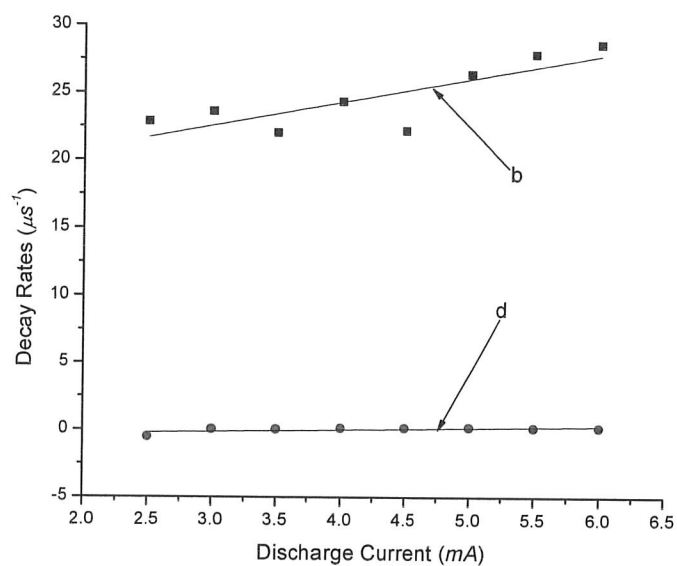


**Fig: 4.13** Plot of decay rates vs discharge current for Xenon 452.6 nm. The solid lines, which pass through the observed data points, are the least square fits to equations (4.2) and (4.3).

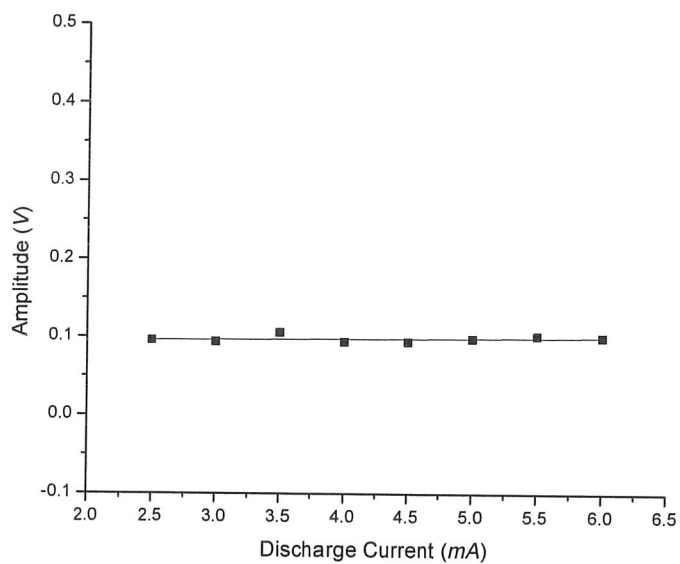


**Fig: 4.14** Plot of the signal amplitude vs discharge current for Xenon 452.6 nm. Here the signal is constant with the increase in discharge current.

Table 4.1

Data for time-resolved OG signals of Xenon at 469.22 nm for different discharge currents.

$I$ (mA)	Fitted Parameters					Amplitude (V) $\pm 0.005$
	$a$ (V) $\pm 0.005$	$b$ ( $\mu\text{s}^{-1}$ ) $\pm 0.005$	$c$ (V) $\pm 0.005$	$d$ ( $\mu\text{s}^{-1}$ ) $\pm 0.005$	$\tau$ ( $\mu\text{s}$ ) $\pm 0.005$	
2	0.416	3.625	-0.014	0.034	0.545	0.085
2.5	0.196	3.691	-0.018	0.058	0.271	0.080
3	0.197	3.679	-0.016	0.047	0.272	0.076
3.5	0.193	3.680	-0.018	0.057	0.271	0.072
4	0.169	3.974	0.017	0.058	0.259	0.068
4.5	0.153	4.117	-0.017	0.057	0.242	0.064
5	0.148	4.278	-0.016	0.055	0.233	0.060
5.5	0.141	4.376	-0.015	0.051	0.228	0.057
6	0.144	4.371	-0.015	0.050	0.228	0.054

Table 4.2

Data for time-resolved OG signals of Xenon at 473.54 nm for different discharge currents.

$I$ (mA)	Fitted Parameters					Amplitude (V) $\pm 0.005$
	$a$ (V) $\pm 0.005$	$b$ ( $\mu\text{s}^{-1}$ ) $\pm 0.005$	$c$ (V) $\pm 0.005$	$d$ ( $\mu\text{s}^{-1}$ ) $\pm 0.005$	$\tau$ ( $\mu\text{s}$ ) $\pm 0.005$	
2	0.310	3.987	-0.020	0.044	0.250	0.154
3	0.355	3.575	-0.022	0.048	0.278	0.152
3.5	0.359	3.644	-0.025	0.059	0.274	0.146
4	0.335	3.773	-0.024	0.058	0.264	0.142
4.5	0.316	3.860	-0.023	0.053	0.258	0.138
5	0.316	3.981	-0.021	0.049	0.249	0.134
5.5	0.310	3.987	-0.020	0.044	0.250	0.132

Table 4.3

Data for time-resolved OG signals of Xenon at 452.6 nm for different discharge currents.

$I$ (mA)	Fitted Parameters					Amplitude (V) $\pm 0.005$
	$a$ (V) $\pm 0.005$	$b$ ( $\mu s^{-1}$ ) $\pm 0.005$	$c$ (V) $\pm 0.005$	$d$ ( $\mu s^{-1}$ ) $\pm 0.005$	$\tau$ ( $\mu s$ ) $\pm 0.005$	
2.5	0.553	20.834	-0.001	-0.535	0.318	0.096
3	0.164	20.578	-0.017	0.043	0.078	0.094
3.5	1.557	21.989	-0.018	0.053	0.504	0.106
4	0.158	20.304	-0.241	0.116	0.056	0.094
4.5	1.187	22.14	-0.135	0.135	0.424	0.094
5	1.404	26.340	-0.023	0.178	0.439	0.098
5.5	1.440	27.799	-0.020	0.147	0.414	0.102
6	1.457	28.548	-0.020	0.159	0.425	0.100

Table 4.4

## Results

Wavelength (nm)	Selection Rule	Collisional Cross Section $mA^{-1}\mu s^{-1}$		$\sigma_k/\sigma_i$	Effective Lifetime $\tau_k (\mu s)$	Maximum Amplitude (V)	Change in Amplitude with Current
		$\sigma_k$	$\sigma_i$				
469.22	$\Delta J = -1$ $\Delta K = 0$	0.23	0.01	23	0.33	0.085	Decreases
473.54	$\Delta J = 1$ $\Delta K = 0$	0.06	-0.05	1.2	0.28	0.154	Decreases
452.6	$\Delta J = 0$ $\Delta K = 0$	1.74	0.14	12.4	0.06	0.106	Constant

## Conclusion

We have studied the time-resolved optogalvanic spectra in the heaviest inert gas i.e. Xenon. A commercial Xenon filled hollow cathode lamp at a pressure of about 1 *mbar* was used for this purpose. We have been able to assess the dominant physical processes responsible for the optogalvanic signal on the basis of a detailed experimental study of the time-resolved optogalvanic spectra in the Xenon discharge plasma. We have chosen following three transitions

$$5p^5 6s[3/2]_2 \rightarrow 5p^5 6p[3/2]_1 \quad \lambda = 469.22 \text{ nm}$$

$$5p^5 6s[3/2]_1 \rightarrow 5p^5 6p[3/2]_2 \quad \lambda = 473.54 \text{ nm}$$

$$5p^5 6s[3/2]_2 \rightarrow 5p^5 6p[3/2]_2 \quad \lambda = 452.6 \text{ nm}.$$

Each of them follow different sets of optical dipole selection rule i.e.  $\Delta J = -1$ ,  $\Delta K = 0$ ,  $\Delta J = 1$ ,  $\Delta K = 0$  and  $\Delta J = \Delta K = 0$ .

First we have scan our dye laser in the region 450.0 to 480.0 *nm* to record these transitions by continuously rotating the grating of the dye laser system using a stepper motor. Time-resolved study was carried out by adjusting the wavelength at the resonance value of the transitions described above. Line shapes of the observed optogalvanic signal have been discussed thoroughly as a function of the discharge current. By using the least square fitting we have found the effective lifetimes of the upper three levels. The values of these lifetimes are also found to be larger than their radiative lifetimes. This is attributed to the radiation trapping in the discharge. The collisional ionization rate parameters of these levels have also been extracted.

Our future task is to study the time-resolved optogalvanic spectra of all possible transitions connecting the  $5p^5 6s$  to  $5p^5 6p$  levels. This will help us to the study in detail the role of the two metastable states in the collisional ionization mechanism for different upper states and also a better comparison between the metastable states and other states can be given.

# BIBLIOGRAPHY

---

- [1] J. A. Rust, J. A. Nobrega, C. P. Calloway Jr, B. T. Jones: *Fraunhofer effect atomic absorption spectrometry*, Anal Chem 2005, **77**, 1060.
- [2] P. Latimer: *Absolute adsorption and scattering spectrophotometry*, Arch Biochem Biophys 1967, **119**, 580.
- [3] G. Racah, Phys. Rev. 1942, **62**, 438.
- [4] R. D. Cowan, 1981, "*The theory of Atomic Structure and Spectra*" University of California Press, Berkeley.
- [5] *A recent comprehensive review of the properties of Rydberg states of atoms and molecules is found in Rydberg States of Atoms and Molecules*, edited by R. F. Stebbings and F. B. Dunning (Cambridge University, Cambridge, 1983).
- [6] T. F. Gallagher 1994, "*Rydberg Atoms*" Cambridge University Press.
- [7] J. E. Bayfield and P. M. Koch, Phys. Rev. 1974 Lett. **33**, 258.
- [8] J. A. Schiavone, D. E. Donohue, D. R. Herrick, and R. S. Freund, Phys. Rev. 1977 A **16**, 48.
- [9] J. Berkawiu 1979, *Photoabsorption, Photoionization and Photoelectron Spectroscopy* (New York Academic).
- [10] P. Camus, M. Dieulin and C. Morillon 1979 J. Phys. Lett. **40**, L513
- [11] R. F. Stebbings, C. J. Latimer, W. P. West, F. B. Dunning, and T. B. Cook 1975, Phys. Rev. A **12**, 1453.
- [12] I. Popescu, C. Ghita, A. Popescu, and G. Musa 1966, Ann. Phys. **18**, 103.
- [13] R. Beigang, K. Lücke, and A. Timmermann 1983, Phys. Rev. A **27**, 587.
- [14] A. P. Thorne 1988 "*Spectrophysics*", 2<sup>nd</sup> Edition-ELBS, Chapman and Hall.
- [15] W. Demtröder 1988, "*Laser Spectroscopy*", Springer Verlag Berlin Heidelberg.
- [16] A. Javan, W. R. Bennett, Jr., and D. R. Herriott 1961, Phys. Rev. Lett. **6**, 106.
- [17] L. F. Johnson 1963, J. Appl. Phys. **34**, 897.
- [18] K. Nassau and G. M. Loiacono 1963, J. Phys. Chem. Solids **24**, 1503.

- [19] T.W. Silfvast 1996, *Laser Fundamentals*.
- [20] N. Bloembergen, *Nonlinear optics*. Reading, MA: W.A. Benjamin, Inc., 1977 (1965). 229 p.
- [21] M. J. Druyvesteyn and F. M. Penning 1940, *Rev. Mod. Phys.* **12**, 87.
- [22] C. Kenty 1950, *Phys. Rev.* **80**, 95.
- [23] K. W. Meissner and W. F. Miller 1953, *Phys. Rev.* **92**, 896.
- [24] R. B. Green, R. A. Keller, G. C. Luther, P. K. Schenck, and J. C. Travis, 1976, *Appl. Phys. Lett.* **29**, 727.
- [25] J. E. Lawler 1980, *Phys. Rev. A* **22**, 1025.
- [26] G. Frez, S. Lavit and E. Miron 1979, *IEEE Quant. Electr.* **15**, 1328.
- [27] A. Ben-Amar, G. Erez and R. Shuker 1983, *J. Appl. Phys.* **54**, 3688.
- [28] R. S. Stewart, K. W. Mcknight and K. I. Hamad 1990, *J. Phys. D: Appl. Phys.* **23**, 832.
- [29] X. L. Han, V. Wisehart, S. E. Conner, M. C. Su and D. L. Monts 1995, *Contrib. Plasma Phys.* **34**, 439.
- [30] P. P. Sorokin and J. R. Lankard 1966, *IBM J. Res. Develop.* **10**, 162.
- [31] F. P. Schäfer, W. Schmidt, J. Volze 1966, *Appl. Phys. Lett.* **9**, 306.
- [32] W. Schmidt, and F. P. Schäfer, *Z. Natur.* 1967, **22a**, 1563.
- [33] B. B. McFarland 1967, *Appl. Phys. Lett.* **10**, 208.
- [34] R. G. Morton, V. C. Draggo 1981, *IEEE J. Quantum Electron.* QE-17, 222.
- [35] O. G. Peterson, S. A. Tuccio, B. B. Snavely, 1970, *App. Phys. Lett.* **17**, 245.
- [36] T. W. Hänsch 1972, *Appl. Opt.* **11**, 895.
- [37] M. H. Miller, R. A. Roig, and G. A. Moo-Young 1971 *Phys. Rev. A* **4**, 971.
- [38] E. D. Stokes, F. B. Dunning, R. F. Stebbings, G. K. Walters, and R. D. Rundel 1972, *Opt. Commun.* **5**, 267.
- [39] D. Hanna, P. Karkainen and R. Wyatt 1975, *Opt. Quantum Electron.* **7**, 115.
- [40] I. Shoshan, N. N. Danon, U. P. Oppenheim 1977, *J. Appl. Phys.* **48**, 4495.
- [41] M. G. Littman and H. J. Metcalf 1987, *Appl. Opt.* **17** 2224.
- [42] F. J. Duarte and J. A. Piper 1982, *Opt. Commun.* **43**, 303.
- [43] F. J. Duarte 1994, *Appl. Opt.* **33**, 3857.



- [44] M. Rifani, Y. -Y Yin, and D. S. Elliott, M. J. Jay, S. -H Jang, M. P. Kelley, L. Bastin, and B. Khar 1995, *Am. J. Chem. Soc.* **117**, 7572.
- [45] I. Braun, G. Ihlein, J. U. Nockel, G. Schulz-Ekloff, F. Schuth, U. Vietze, O. Wieb and D. Wöhrle 2000, *Appl. Phys. B* **70**, 335.
- [46] N. E. Small-Warren and L. Y. C. Chiu 1975, *Phys. Rev. A* **11**, 1777.
- [47] S. Mahmood, M. Anwar-ul-Haq, M. Riaz, M. A. Baig 2004, *Optics Commun.* **236**, 411.
- [48] L. Allen, D. G. C. Jones, and D. G. Schofield, *J. Opto. Society of America*, **59**, 7.
- [49] T. Fujimoto, C. Goto and K. Fukuda 1982, *Phys. Scr.* **26**, 443.